Synthesis and characterization of novel diamino ligand precursors bearing diversified functionalized linker frameworks

Abstract

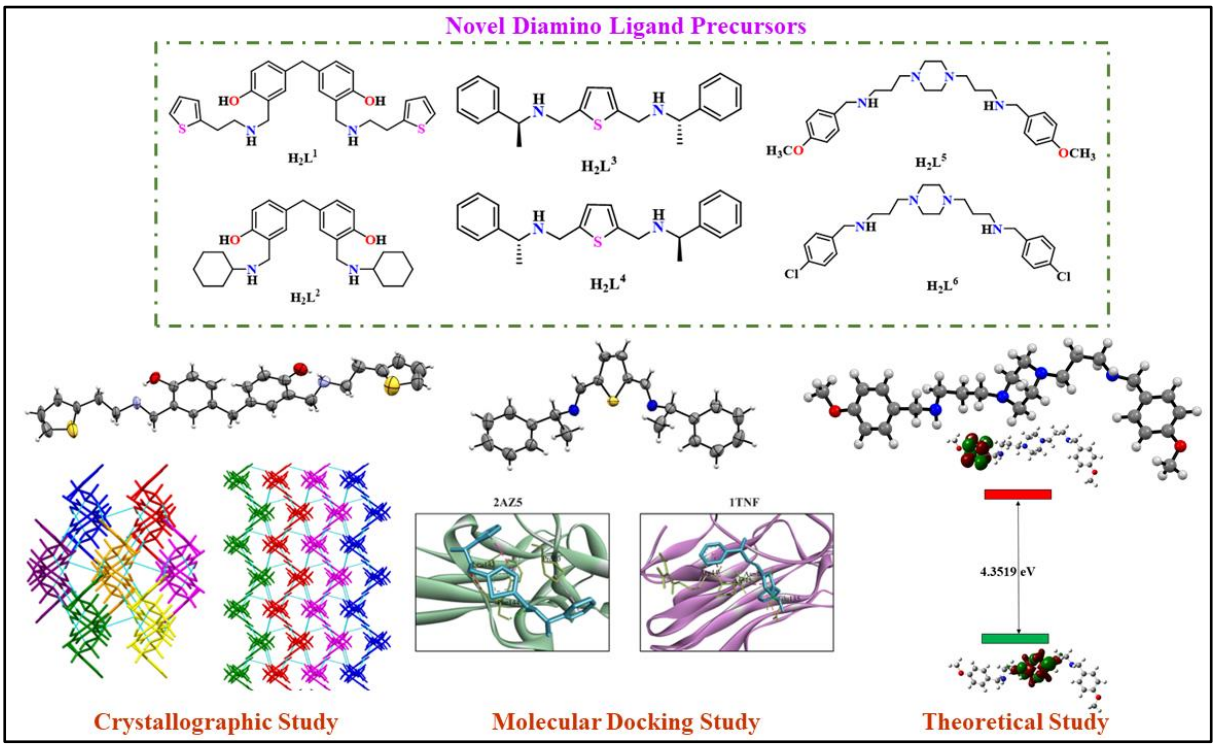

The novel secondary diamines *viz.* 4,4'-methylenebis-2-((2-thiophen-2-yl)ethylamino)methylphenol (**H_2L^1**), 4,4'-methylenebis-2-(cyclohexylamino)methylphenol (**H_2L^2**), S,S-(Thiophene-2,5-diyl)bis(N-(1-phenylethyl)methanamine) (**H_2L^3**), R,R-(Thiophene-2,5-diyl)bis(N-(1-phenylethyl)methanamine) (**H_2L^4**), *N*,*N*′-bis{3-(*p*-methoxybenzylamino)propyl}piperazine (**H_2L^5**) and *N*,*N*′-bis{3-(p-chlorobenzylamino)propyl}piperazine (**H_2L^6**) holding diversified functionalized linkers have been synthesized in this chapter. The formation and purity of all the compounds were verified by microanalysis and standard spectroscopic methods such as NMR, IR, SCXRD and supported by density functional theory calculations. The unambiguous molecular structure of some of the representative compounds synthesized in this chapter were determined means of single crystal XRD and their crystal packing patterns were studied.

2.1 Introduction

There is growing research in the development of novel imines and amines[1] due to their prevalent applications in research laboratories and industries for the synthesis of fine chemicals used ubiquitously in biology, dyes, agrochemicals, surfactants and lubricants.[2] In particular, approximately 42% of drugs and drug candidates contain amine functional groups in their molecular structures.[3] For instance, amongst well established drugs containing amino groups: chlorpheniramine is an antihistamine drug helping in releasing allergic ailments caused by cold, fever, itchy skin, insect bites whereas chlorpromazine is used to relieve nervousness, excitement, and even mental disorder. Several secondary amines *viz.* nortriptyline, desipramine, and amoxapine, apart from tertiary amines amitriptyline, imipramine, lofepramine and clomipramine are used as an antidepressants drug. Further reports demonstrate that substituted tryptamines and phenethylamines are key basic structures for a large variety of psychedelic drugs. Well known anesthetics such as morphine, codeine, and heroin contain tertiary amino groups. The US DEA has listed amphetamine, methamphetamine and methcathinone amines as controlled substances for psychostimulant. The chiral amines viz. ephedrine and phenylephrine are used to relieves congestion. Presumably, the amine moieties in the organic drugs helps in an active transportation of drug through the formation of organic ammonium cation.

A structural combination of diaminodiphenylmethane along with hydrophobic substituents on the nitrogen atoms in GN8 derivatives is responsible for the antiprion activity in TSE-infected cells.[4] The flexibility associated with diaminodiphenylmethane has led to the formation of binuclear macrocyclic dithiocarbamate complexes bearing functionalized linker framework.[5]

Apart from this, chirality has been playing an important role in the modern drug development because therapeutic activity of enantiomers differs severely in terms of toxicity and pharmacokinetics.[6] Recently, we have demonstrated on how chirality and redox potentials of enantiomers influences their anti-proliferative activity.[7] The chiral molecules present in the biological system (proteins) apparently recognise the enantiomers selectively and assist in the improved biological activity through ligand-protein bonding.[7, 8]

Moreover, Tumor Necrosis Factor Alpha (TNF-α) is a pleiotropic pro-inflammatory cytokine. It acts as central biological regulator in critical immune functions, but its dysregulation has been linked with a number of diseases. Inhibition of TNF-α has considerable therapeutic potential for diseases such as cancer, diabetes, and especially autoimmune diseases.[9]

Physiologically it is an important regulator of immune functions, but its dysregulation has been linked with cancer, neurological diseases and especially autoimmune diseases.[10, 11] Researchers have developed ligand based selective pharmacophore model to perform virtual screening of plant origin natural product database for the identification of potential inhibitors against TNF-α. The ligands selected through virtual screening were further verified by using an in vitro assay displaying the most promising inhibitory activity in low micro molar concentration.[9] This has encouraged several researchers to perform virtual screening of small molecules *via* molecular docking study.[12]

Several efficient methods have been optimized *viz.* catalysis,[13] Ullmann reactions,[14] Buchwald−Hartwig amination[15] and reductive amination reactions[16] to develop the synthesis of various amino compounds holding functionalised organic frameworks. Imines are broadly used as a suitable precursor for secondary amines that are essential pharmacophore in numerous biologically active compounds[1b, 16] and further utilized in the synthesis of sulphur-rich dithiocarbamate ligands and their complexes.[17]

Besides, the piperazines have been proven as important class of organic compounds and versatile building block for designing new materials with tailored physicochemical[18] and biological properties.[19] While a number of synthesis routes of 1,4-disubstituted piperazines are available in the literature,[20] however, reported routes majorly suffers from low yields, time consuming, harsh reaction conditions and side reactions. The synthesis of 1,4-disubstituted piperazines is an active area of research in the supramolecular chemistry as piperazine unit provides additional opportunity for weak interactions, generate a scope for sophisticated manipulation in the crystal packing and hence supramolecular architectures. In recent times, piperazine derivatives have also been developed as CO_2 capturing materials.[21] Moreover, substituted piperazines have displayed potentials as an antimalarial[22a] and anthelmintic[22b, 22c] drugs and to some extent towards tumorigenicity or mutagenicity.

Furthermore, piperazinyl linked ciprofloxacine dimers and other derivatives of piperazine are appeared as potent antibacterial agents against resistant strains, dual calcium antagonist, antimalarial agents, antifungal agents and potential antipsychotic agents.[23] However, dithiocarbamate derivatives of functionalized piperazine and their transition metal complexes are far less studied.[19d, 24]

Thus, in order to explore the scope of new diamino compounds for further derivatisation, we have designed and synthesized a number of diamino precursors such as 4,4'-methylenebis-2-((2-thiophen-2-yl)ethylamino)methylphenol (**H_2L^1**), 4,4'-methylenebis-2-(cyclohexylamino)methylphenol (**H_2L^2**), *S,S*-(Thiophene-2,5-diyl)bis(N-(1-phenylethyl)-

methanamine) (**H$_2$L^3**), *R*,*R*-(Thiophene-2,5-diyl)bis(N-(1-phenylethyl)methanamine) (**H$_2$L^4**), *N*,*N*′-bis{3-(*p*-methoxybenzylamino)propyl}piperazine (**H$_2$L^5**) and *N*,*N*′-bis{3-(p-chlorobenzylamino)propyl}piperazine (**H$_2$L^6**) holding varied linker frameworks (Chart 1) and these were structurally characterized prior to use in the development of their ensuing transition metal dithiocarbamate derivatives.

All the functionalized organic diamines were characterized thoroughly by Elemental analysis, NMR (^{1}H and ^{13}C), UV-visible, FTIR and single crystal X-ray diffraction (SCXRD) techniques. The experimental outcomes of these molecules have been further investigated by theoretical calculations.

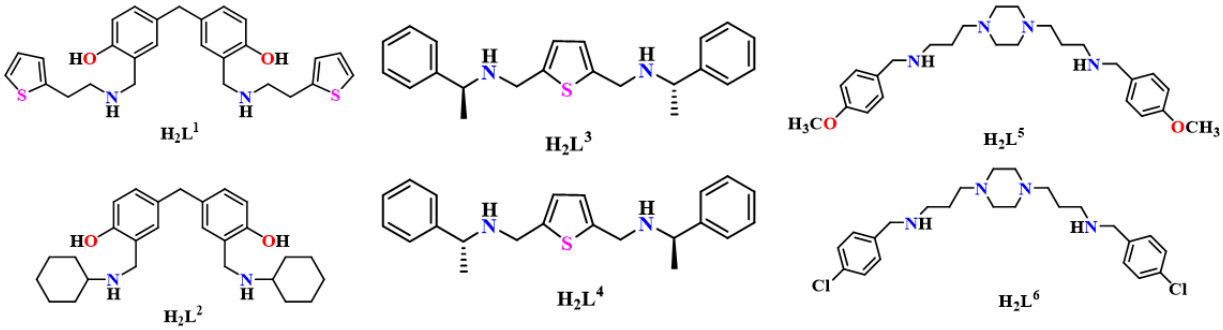

Chart 1. List of novel diamino ligand precursors under investigation.

2.2 Experimental Section

2.2.1 Materials and Instrumentation

Solvents were purchased from the commercial sources and were freshly distilled prior to use. Reagents were procured from Merck and Sigma-Aldrich Chemicals Limited; these were used without further purification. Thin Layer Chromatography was performed on Merck 60 F254 aluminium coated plates to monitor the progress of reaction. The NMR experiments were carried out on a Bruker AV-III 400 MHz spectrometer in spectrometer with $CDCl_3$ and TMS as internal standard. FT-IR spectra were recorded in the 4000-400 cm^{-1} range using a Bruker FT-IR spectrometers as KBr pellets. UV-visible absorption spectra were recorded on a JASCO V-730 UV-visible spectrophotometer. All the geometry optimizations were performed with the Gaussian 16 program and molecular orbitals were generated using GaussView 6.0 program.

2.2.2 General procedure for the synthesis of bisimine and diamine precursors holding diphenylmethane linker

2.2.2.1 Synthesis of bisimines BI-1 and BI-2

5,5'-methylenebis(2-hydroxybenzaldehyde) (1.0 g, 3.90 mmol) was dissolved in a CH_2Cl_2:MeOH (50:200 v/v, ml) mixture and 2-(thiophen-2-yl)ethan-1-amine (0.99 g, 7.81 mmol) or cyclohexylamine (0.77 g; 7.81 mmol) was added drop wise into this solution. After the addition the resultant mixture was stirred at room temperature for one hour. The reaction mixture was concentrated under vacuum using rotary evaporator. The product was purified by column chromatography (CH_2Cl_2:Methanol). The product was dried under high vacuum to yield the corresponding products **BI-1** and **BI-2**.

2.2.2.2 Synthesis of diamines H_2L^1 and H_2L^2

Bis-imino derivative **BI-1** (1g, 2.1 mmol) or **BI-2** (1g, 2.3 mmol) was dissolved in methanol. Sodium borohydride (0.159g, 4.2mmol) was added to the methanolic solution of bisimines and stirred for 2 hours at room temperature. After the reduction, the solvent was evaporated under vacuum using a rotary evaporator. Resultant solid was quenched in water. The product was extracted in dichloromethane. The dichloromethane layer was dried with anhydrous sodium sulphate, and concentrated to get the free flowing bis-methylaminoderivatives **H_2L^1** and **H_2L^2**.

2.2.3 General procedure for the synthesis of bisimine and diamine precursors holding thiophene linker

2.2.3.1 Synthesis of bisimines BI-3 and BI-4

A solution of 2,5-thiophenedicarboxaldehyde (0.14 g, 1 mmol) prepared in 20 mL methanol was added into a 20 mL methanolic solution of or S-(-)-1-phenylethylamine (0.24 g, 2 mmol) or R-(+)-1-phenylethylamine (0.24 g, 2 mmol). The formation of pale-yellow residue was observed after an hour and the reaction was allowed to continue at room temperature for three hours. The residue was filtered and washed by methanol followed by n-hexane. The residue was dried under high vacuum to yield the corresponding products **BI-3** and **BI-4**.

2.2.3.2 Synthesis of diamines H_2L^3 and H_2L^4

To a stirred solution of **BI-3** (0.34 g, 1 mmol) or **BI-4** (0.34 g, 1 mmol) in dichloromethane (30 mL), added a dichloromethane solution of sodium triacetoxyborohydride (1.27 g, 6 mmol). Reaction mixture was allowed to stir at room temperature for three hours, within an interval of 30 minutes a reaction progress was monitored by thin layer chromatography. After

completion of reaction, the solvent was removed under reduced pressure using rotatory evaporator and the product was extracted by dichloromethane using a solvent extraction technique and dried in rotary evaporator. The corresponding products **H_2L^3** and **H_2L^4** were stored under nitrogen atmosphere and data were collected.

2.2.4 General procedure for the synthesis of bisimine and diamine precursors holding piperazine linker

Both the bisimines **BI-5** and **BI-6** and their reduced diamine products H_2L^5 and H_2L^6 have been prepared by following a modified literature procedure[25] as described below.

2.2.4.1 Synthesis of bisimines BI-5 and BI-6

A 20 mL methanolic solution of p-methoxybenzaldehyde (0.14 g, 2 mmol) or p-chlorobenzaldehyde (0.14 g, 2 mmol) was added dropwise to a methanolic solution (20 mL) of 1,4-bis(3-aminopropyl)piperazine (0.2 g, 1 mmol). The reaction mixture was allowed to stir for 6 hours. The complete reaction progress is monitored by a TLC method. The reaction mixture was allowed to dry over sodium sulphate for several hours, filtered and the solvent was evaporated under the vacuum to yield the products **BI-5** and **BI-6** which were stored under nitrogen atmosphere for analysis.

2.2.4.2 Synthesis of diamines H_2L^5 and H_2L^6

A solution of sodium borohydride (0.075 g, 2 mmol) in 20 ml MeOH was added dropwise to a stirred solution of *N*,*N*′-bis{3-(*p*-methoxybenzylideneamino)propyl}piperazine **BI-5** (0.44 g, 1 mmol) or *N*,*N*′-bis{3-(*p*-chlorobenzylideneamino)propyl}piperazine **BI-6** (0.46 g, 1 mmol) in 30 ml MeOH at room temperature. The reaction mixture was allowed to stir for three hours and the reaction progress was observed with TLC periodically. The reaction mixture was quenched by dropwise addition of water (20 mL) and MeOH was removed under reduced pressure. The product was extracted from the aqueous mixture with CH_2Cl_2 (4 × 25 mL) by using a solvent extraction technique and dried in rotary-evaporator. The corresponding products **H_2L^5** and **H_2L^6** were stored under nitrogen atmosphere for data collection.

Table 1. Micro-, mass- and IR analysis data for compounds **BI-1-BI-6** and **H_2L^5-H_2L^6.**

Entry	Molecular Formula	Molecular Weight	Yield (%)	M.P. (°C)	Elemental Analysis % Found calculated				IR data (KBr disk) υ_{max}/cm^{-1}
					C	H	N	S	
BI-1	$C_{27}H_{26}N_2O_2S_2$	474.64	96	88	68.39 68.33	5.58 5.52	5.95 5.90	13.57 13.51	3375(w), 3011(w), 2660(w), 2532(w), 1638(vs), 1584(s), 1490(vs), 1457(w), 1436(w), 1397(w), 1369(w), 1341(w), 1278(s), 1227(s), 1154(w), 1035(w), 966(w), 926(w), 847(w), 813(s), 697(s), 619(w), 565(w), 504(w), 470(w), 437(w)
BI-2	$C_{27}H_{34}N_2O_2$	418.58	94	96	77.55 77.48	8.24 8.19	6.73 6.69	-	3401(w), 2928(vs), 2862(s), 1630(vs), 1585(s), 1488(vs), 1444(w), 1380(w), 1346(w), 1277(s), 1213(w), 1156(w), 1127(w), 1078(s), 974(w), 928(w), 892(w), 820(s), 772(w), 625(w), 570(w), 497(w), 427(w)
BI-3	$C_{22}H_{22}N_2S$	346.49	92	164	76.34 76.26	6.46 6.40	8.16 8.09	9.31 9.25	3058 (w), 3033 (s), 2969 (s), 2924 (w), 2863 (s), 1622 (vs), 1489 (w), 1452 (s), 1375 (s), 1341 (w), 1309 (s), 1231 (s), 1199 (w), 1117 (w), 1082 (s), 1056 (s), 1026 (w), 1009 (w), 998 (w), 951 (s), 825 (s), 766 (s), 698 (vs), 522 (s), 414 (w)
BI-4	$C_{22}H_{22}N_2S$	346.49	90	160	76.35 76.26	6.48 6.40	8.15 8.09	9.32 9.25	3033 (w), 2969 (s), 2924 (w), 2863 (s), 1622 (vs), 1489 (w), 1451 (s), 1374 (s), 1341 (w), 1310 (s), 1230 (s), 1200 (w), 1117 (s), 1082 (w), 1056 (w), 1026 (w), 1009 (w), 998 (w), 951 (s), 908 (w), 825 (w), 766 (s), 698 (s), 556 (w), 541 (w), 522 (s), 414 (w)
BI-5	$C_{26}H_{36}N_4O_2$	436.60	94	89	71.59 71.53	8.36 8.31	12.87 12.83	-	3403(w), 3251(w), 3031(w), 2998 (w), 2933 (s), 2871(s), 2826(w), 1639(s), 1604(s), 1575(s), 1511(s), 1468(w), 1441(w), 1418(w), 1384(w), 1357(w), 1303(s), 1277(w), 1241(vs), 1180(w), 1163(s), 1140(w), 1109(w), 1051(s), 1024(w), 995(w), 960(w), 937(w), 877(w), 840(s), 819(w), 768(w), 676(w), 633(w), 597(w), 534(w), 516(w)
BI-6	$C_{24}H_{30}Cl_2N_4$	445.43	90	92	64.76 64.72	6.85 6.79	12.62 12.58	-	3428(w), 3274(w), 3049(w), 3021(w), 2935(s), 2874(w), 2851(w), 2822(s), 2771(w), 2672(w), 1645(s), 1591(s),

									1568(w), 1552(w), 1487(s), 1463(w), 1444(w), 1398(w), 1373(w), 1345(s), 1312(s), 1294(w), 1277(w), 1240(w), 1216(w), 1192(w), 1157(s), 1142(w), 1084(vs), 1015(s), 976(s), 958(w), 938(w), 898(w), 828(s), 777(w), 751(s), 698(w), 629(w), 608(w), 582(s), 508(s), 487(w), 434(w)
H_2L^1	$C_{27}H_{30}N_2O_2S_2$	478.67	92	105	67.83 67.75	6.39 6.32	5.91 5.85	13.52 13.40	3476(w), 3259(vs), 2895(s), 2823(s), 2611(w), 1792(w), 1602(s), 1499(s), 1461(w), 1436(w), 1407(w), 1339(w), 1251(s), 1217(w), 1180(w), 1151(w), 1112(s), 1046(w), 994(s), 924(w), 896(w), 874(w), 832(s), 812(s), 768(w), 688(vs), 647 (w), 610(w), 556(w), 509(w), 454(w)
H_2L^2	$C_{27}H_{38}N_2O_2$	422.61	91	120	76.79 76.74	9.10 9.06	6.68 6.63	-	3425(w), 3266(s), 2928(s), 2851(s), 1600(s), 1497(s), 1462(w), 1405(w), 1370(w), 1311(w), 1250(s), 1215(w), 1148(w), 1107(s), 1010(w), 965(w), 918(w), 890(w), 838(s), 816(w), 788(w), 765(w), 651(w), 614(w), 558(w), 509(w), 459(w), 431(w)
H_2L^3	$C_{22}H_{26}N_2S$	350.52	85	-	75.43 75.38	7.52 7.48	8.04 7.99	9.23 9.15	3322 (w), 3064 (w), 3025 (s), 2967 (w), 2820 (s), 1450 (s), 1363 (w), 1206 (w), 1116 (s), 1024 (w), 914 (w), 802 (w), 762 (s), 702 (s), 544 (m)
H_2L^4	$C_{22}H_{26}N_2S$	350.52	80	-	75.44 75.38	7.53 7.48	8.07 7.99	9.21 9.15	3329 (w), 3060 (w), 3025, 2964 (s), 2924 (w), 2823 (w), 1492 (s), 1450 (s), 1369 (w), 1304 (w), 1205 (w), 1117 (s), 1027 (w), 803 (w), 761 (s), 700 (s), 587 (w), 545 (w)
H_2L^5	$C_{26}H_{40}N_4O_2$	440.63	88	-	79.93 79.87	9.19 9.15	12.77 12.72	-	3265(w), 2999(w), 2938(s), 2824(s), 1640(w), 1609(s), 1581(w), 1512(s), 1462(s), 1380(w), 1356(w), 1301(w), 1246(s), 1177(s), 1111(w), 1030(s), 972(w), 939(w), 819(s), 777(w), 704(w), 635(w), 575(w), 521(w)
H_2L^6	$C_{24}H_{34}Cl_2N_4$	449.46	85	-	64.19 64.14	7.67 7.63	12.53 12.47	-	3294(s), 3049(w), 2940(s), 2866(w), 2800(vs), 2759(s), 2671(w), 1896(w), 1789(w), 1736(w), 1642(w), 1594(w), 1572(w), 1488(s), 1470(w), 1450(vs), 1400(w), 1373(w), 1349(s), 1311(s), 1269(s), 1253(w), 1195(w), 1162(s), 1123(s), 1087(vs), 1035(w), 1010(s), 982(s), 939(w), 881(w), 812(vs), 794(s), 759(w), 693(w), 671(s), 638(w), 521(w), 481(s)

Table 2. NMR spectral data for compounds **BI-1**-**BI-6** and **H_2L^5**-**H_2L^6.**

Entry	NMR Data (ppm)	
	^{1}H NMR ($CDCl_3$)	**^{13}C NMR ($CDCl_3$)**
BI-1	13.23 (s, 2H, -O*H*); 8.24 (s, 2H, -C*H*=N-); 6.86-7.28 (m, 12H, Ph and Th); 3.88 (s, 2H, Ph-CH_2-Ph); 3.86 (t, 4H, =N-CH_2-); 3.24 (t, 4H, -CH_2Th)	-
BI-2	13.72 (s, 2H, -O*H*); 8.31 (s, 2H, -C*H*=N-); 6.89-7.28 (d, 6H, Ph); 3.92 (s, 2H, Ph-CH_2-Ph); 3.19 (m, 2H, C*H* of Cy); 1.58-1.85 (m, 20 H, CH_2- of Cy)	-
BI-3	8.40 (s, 2H, -C*H*=N); 7.24-7.44 (m, 12H, aromatic protons); 4.52 (q, J_{H-H} = 6.4 Hz, 2H, -C*H*); 1.58 (d, J_{H-H} = 6.4 Hz, 6H, -CH_3)	152.5, 145.2, 145.0, 129.9, 128.5, 126.9, 126.6, 69.4, 25.1
BI-4	8.40 (s, 2H, -C*H*=N); 7.24-7.44 (m, 12H, aromatic protons); 4.52 (q, J_{H-H} = 6.8 Hz, 2H, -C*H*); 1.59 (d, J_{H-H} = 6.8 Hz, 6H, -CH_3)	152.5, 145.2, 145.0, 129.9, 128.5, 126.9, 126.6, 69.4, 25.1
BI-5	8.20 (s, 2H, -C*H*=N), 6.91-7.66 (m, 8*H*, -Ph), 3.83 (s, 6H, -OCH_3), 3.59 (t, J_{H-H} = 6.8 Hz, 4H, -C=N-CH_2), 2.43-2.40 (m, 12*H*, -NCH_2), 1.91-1.84 (m, 4H, -N-CH$_2$-CH_2)	161.5, 160.6, 129.6, 129.1, 113.9, 77.4, 77.1, 76.8, 59.6, 56.3, 55.4, 53.2, 28.1
BI-6	8.24 (s, 2H, Ph-C*H*=N-), 7.37-7.66 (m, 8H, -Ph), 3.62-3.65 (t, J_{H-H} = 6.8 Hz, 4H, -C=N-CH_2), 2.47-2.43 (m, 12*H*, -NCH_2), 1.94-1.86 (m, 4H, -N-CH$_2$-CH_2)	159.9, 136.5, 134.6, 130.9, 130.9, 129.5, 129.2, 128.9, 128.0, 59.6, 56.2, 53.0, 27.9
H_2L^1	6.76-7.28 (m, 12H, Ph/Th); 3.95 (s, 2H, Ph-CH_2-Ph); 3.77 (s, 4H, Ph-CH_2-NH); 3.08 (t, 4H, -CH_2NH); 2.98 (t, 4H, -CH_2Th)	156.3, 141.5, 132.2, 129.0, 128.6, 127.1, 125.5, 123.9, 122.2, 116.3, 52.5, 49.7, 40.2, 29.8
H_2L^2 (DMSO-d_6)	6.87 (d, 4H, *Ph*); 6.55 (d, 2H, *Ph*); 3.804 (s, 2H, Ph-CH_2-Ph); 3.64 (merged s, 4H, -NHCH_2); 2.32 (m, 2H, -C*H* of Cy); 1.16-1.84 (m, 20 H, CH_2 of Cy)	-
H_2L^3	7.28-7.39 (m, 10 H, *Ph*); 6.70 (s, 2H, -thiophene); 3.93 (m, 2H, -C*H*); 3.75 (s, 4H, -CH_2); 3.10 (s, 2H, -N*H*); 1.40 (d, J_{H-H} = 6.8 Hz, 6H, -CH_3)	144.7, 142.8, 128.6, 127.2, 126.8, 124.7, 56.9, 46.1, 23.9
H_2L^4	7.28-7.39 (m, 10H, *Ph*); 6.70 (s, 2H, -thienyl-H); 3.91 (m, 2H, -C*H*); 3.75 (s, 4H, -NCH_2); 2.62 (s, 2H, -N*H*); 1.40 (d, J_{H-H} = 6.8 Hz, 6H, -CH_3)	144.4, 142.1, 127.8, 126.0, 125.7, 123.5, 55.9, 45.2, 23.2
H_2L^5	7.28-6.85 (m, 8H, -P*h*), 3.81 (s, 6H, -OCH_3), 3.72 (s, 4H, PhCH_2), 2.67-2.64 (t, 4H, -NHCH_2), 2.41-2.37 (m, 12*H*, -NCH_2)**,** 2.15 (s, br, 2H, N*H*), 1.74-1.67 (m, 4H, -N-CH$_2$-CH_2)	158.6, 132.5, 129.3, 113.8, 56.9, 55.3, 53.4, 53.2, 47.9, 26.9
H_2L^6	7.30-7.24 (m, 8H, -Ph), 3.74 (s, 4H, Ph-CH_2), 2.67-2.63 (t, 4H, -NHCH_2), 2.40-2.37 (m, 12*H*, -NCH_2)**,** 2.05 (s, 2H, N*H*), 1.73-1.66 (m, 4H, -N-CH$_2$-CH_2)	138.9, 132.5, 129.4, 128.5, 57.9, 53.3, 48.1, 26.8

2.2.5 Molecular docking study

2.2.5.1 Ligand preparation

The 3D structures of certain ligands were extracted from optimized structure in Gaussian 16.0 in PDB format and they were assigned charges and torsions and converted to PDBQT in autodock vina.

2.2.5.2 Protein preparation and Grid Parameters

The protein Tumor Necrosis Factor Alpha with PDB ID: 1TNF and 2AZ5 is downloaded from RCSB Protein Data Bank. The protein was prepared by Discovery Studio Client 21. The grid co-ordinates were assigned within the 3D space of ligand for 1TNF and 2AZ5 by autodock vina. The docking protocol is validated by re-docking the ligand onto the active site of receptor pocket.[26] The binding site of the protein was predicted by Discovery Studio Visualizer 21. The assigned Grid Co-ordinates of the active site X: 34.948322 Y: 58.626136 Z: 47.521359, the ligands were also blind docked with complete Chain-A of 1TNF and 2AZ5 as binding pocket.

2.2.5.3 Validation of Docking

The docking of ligands onto the binding site of protein is executed and docking was performed using autodock vina. The ligands were screened for their efficient fitting into the receptor (minimized) grid. The ligands were screened with all possible minimum energy confirmations. The non-bonding interactions within 6 Å of active site of receptor pocket is explored using Discover Studio Visualizer 21.[27] Visualization of residues Interaction. Non-bonding interactions of all ligands with protein were elucidated using Discovery Studio Client 21. The binding interactions of ligands with active site of protein were compared with that of ligand with binding energy.

2.3 Result and Discussion

2.3.1 Bisimines BI-1, BI-2 and diamines H_2L^1, H_2L^2

2.3.1.1 Synthesis and characterization

The bisimines 4,4'-methylenebis(2-((Z)-((2-(thiophen-2-yl)ethyl)imino)methyl)phenol) **BI-1**, 4,4'-methylenebis(2-((Z)-(cyclohexylimino)methyl)phenol) **BI-2** were synthesized under a mild reaction condition with >90 % yields by condensation of 5,5'-methylenebis(2-hydroxybenzaldehyde) with 2-(thiophen-2-yl)ethan-1-amine or cyclohexylamine (Scheme 1). These bisimines were conveniently reduced to their diamine products 4,4’-methylenebis-2-((2-thiophen-2-yl)ethylamino)methylphenol **H_2L^1** and 4,4’-methylenebis-2-

(cyclohexylamino)methylphenol **H_2L^2** at room temperature with sodium borohydride in dichloromethane with >90 % yields.

The microanalysis data for **BI-1**, **BI-2**, **H_2L^1** and **H_2L^2** are consistent with their compositions and confirms their purity which is corroborated by subsequent spectral study.

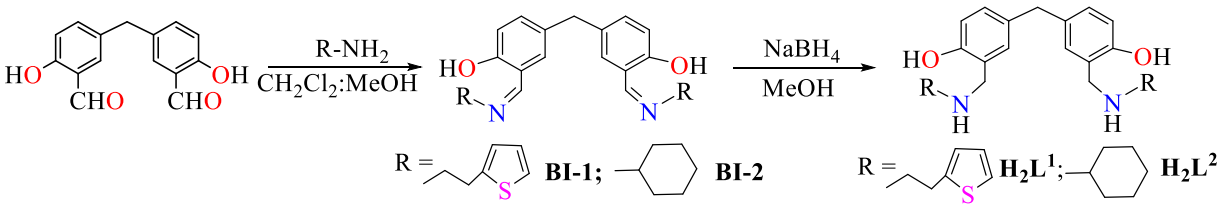

Scheme 1: Synthesis of new bisimines **BI-1, BI-2** and diamines **H_2L^1, H_2L^2** holding diphenylmethane spacers.

The ^{1}H NMR spectra of bisimines **BI-1** and **BI-2** gave most characteristic signal at 8.23 ppm and 8.31 ppm as singlet due to C*H*=N moiety which vanished in their reduced products and confirms the formation of corresponding diamines **H_2L^1** and **H_2L^2**. Notably, the protons of cyclohexyl group of **BI-2** gave signals in the region of 1.58-1.85 ppm and appeared upfield at 1.16-1.84 ppm in **H_2L^2**. Moreover, bisimines gave all the aromatic signals in the expected range of 6.86-7.28 ppm.

The IR spectra of bisimines **BI-1** and **BI-2** exhibit a characteristic band that can be assigned to υ(C=N) ~1638 cm^{-1}. Remarkably, at this band is absent from the spectra of respective diamines. The diamines **H_2L^1** and **H_2L^2** displayed υ(N-H) bands in the region of 3259–3266 cm^{-1}. Due of the aromatic υ(C-H) stretching vibrations, all of the compounds produced mild intensity bands in the 2823–2895 cm^{-1} and 2851–2928 cm^{-1} regions, as well as a very strong band in the 832–838 cm^{-1} area because of the aromatic υ(C-H) out-of-plane bending vibrations.

2.3.1.2 X-ray Crystallographic Study

The single crystals of diamine **H_2L^1** suitable for single crystal X-ray diffraction (SCXRD) study were grown by slow evaporation from dichloromethane solution. The diamine **H_2L^1** crystallize in the monoclinic $P2_1/C$ space group. The X-ray crystal structures of **H_2L^1** is shown in Figure 2. The crystallographic data and structure parameters for **H_2L^1** are given in Table 3.

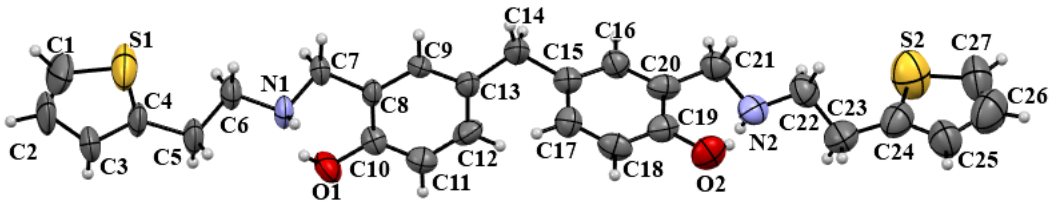

Figure 1. X-ray structure $\mathbf{H_2L^1}$ with atom numbering scheme.

Table 3. Crystal data and structure parameters for the diamine $\mathbf{H_2L^1}$.

Identification code	$\mathbf{H_2L^1}$
CCDC Number	2248632
Empirical formula	$C_{27}H_{30}N_2O_2S_2$
Formula weight	478.65
Temperature/K	293(2)
Crystal system	monoclinic
Space group	$P2_1/c$
a/Å	52.168(4)
b/Å	5.3385(5)
c/Å	9.0194(9)
α/°	90
β/°	91.653(7)
γ/°	90
Volume/Å^3	2510.8(4)
Z	4
ρ_{calc}g/cm^3	1.266
μ/mm^{-1}	0.239
F(000)	1016.0
Crystal size/mm^3	0.57 × 0.48 × 0.47
Radiation	Mo Kα (λ = 0.71073)
2Θ range for data collection/°	7.032 to 58.172
Index ranges	$-69 \le h \le 70$, $-7 \le k \le 7$, $-12 \le l \le 12$
Reflections collected	51380
Independent reflections	6249 [R_{int} = 0.0826, R_{sigma} = 0.0554]
Data/restraints/parameters	6249/0/327
Goodness-of-fit on F^2	1.032
Final R indexes [I>=2σ (I)]	R_1 = 0.1185, wR_2 = 0.3144
Final R indexes [all data]	R_1 = 0.2171, wR_2 = 0.3981
Largest diff. peak/hole / e Å^{-3}	0.59/-0.56

Table 4 presents the selected structural parameters, such as bond lengths and bond angles. These values have been published before and have been determined to be consistent. Density functional theory calculations have been used to optimize the geometry of each molecule to

verify the outcomes of the experiments. A careful comparison of selected structural parameters tells that calculated bond lengths in **H_2L^1** viz. N_{amine}-C_{CH2}= 1.490 Å, $O_{Phenolic}$-C_{Phenyl} = 1.382 Å and C_{Phenyl}-$C_{Methylene}$ = 1.523 Å are pointedly overestimated which are comparable to the similar parameters obtained experimentally. Moreover, calculated angles are found to be consistent with the experimentally determined similar parameters. Thus, Table 4 provides an in-depth analysis of experimental bond lengths (Å) and bond angles (º) with the theoretical values derived from DFT calculations for each compound.

Table 4. Comparision of experimetal bond lengths (Å) and bond angles (º) with theoretical value obtained by DFT calculations.

Entry	Selected Bond	Bond Length (Å)	Selected Bond	Bond angle (º)
Experimental data obtained from SCXRD				
H_2L^1	N1-C7	1.462(6)	C6-N1-C7	113.6(3)
	O1-C10	1.364(5)	O1-C10-C8	119.7(3)
	C13-C14	1.507(6)	C13-C14-C15	117.0(4)
Theoretical data obtained from DFT				
BI-1	N_{imine}-C_{CH2}	1.299	C_{CH2}-N_{imine}-C_{CH2}	120.64
	$O_{Phenolic}$-C_{Phenyl}	1.363	$O_{Phenolic}$-C_{Phenyl}-C_{Phenyl}	121.38
	C_{Phenyl}-$C_{Methylene}$	1.522	C_{Phenyl}-$C_{Methylene}$-C_{Phenyl}	114.78
BI-2	N_{imine}-C_{CH2}	1.298	C_{Cy}-N_{imine}-C_{CH2}	120.86
	$O_{Phenolic}$-C_{Phenyl}	1.364	$O_{Phenolic}$-C_{Phenyl}-C_{Phenyl}	121.38
	C_{Phenyl}-$C_{Methylene}$	1.522	C_{Phenyl}-$C_{Methylene}$-C_{Phenyl}	114.82
H_2L^1	N_{amine}-C_{CH2}	1.490	C_{CH2}-N_{amine}-C_{CH2}	115.22
	$O_{Phenolic}$-C_{Phenyl}	1.382	$O_{Phenolic}$-C_{Phenyl}-C_{Phenyl}	121.31
	C_{Phenyl}-$C_{Methylene}$	1.523	C_{Phenyl}-$C_{Methylene}$-C_{Phenyl}	115.01
H_2L^2	N_{amine}-C_{CH2}	1.490	C_{Cy}-N_{amine}-C_{CH2}	116.44
	$O_{Phenolic}$-C_{Phenyl}	1.382	$O_{Phenolic}$-C_{Phenyl}-C_{Phenyl}	121.34
	C_{Phenyl}-$C_{Methylene}$	1.523	C_{Phenyl}-$C_{Methylene}$-C_{Phenyl}	114.94

In particular, asymmetric unit of **H_2L^1** contains one molecule in the unit cell which offers a number of intra- and intermolecular H-bonding interactions. For instance, N-H and O-H functionalities of **H_2L^1** behaves as donor as well as acceptor H-bonding sites, forming intramolecular H-bonding via O1-H1…N1 (1.881 Å) and O2-H2…N2 (1.981 Å) and intermolecular H-bonding closing contacts via N1-H1A…O1 (2.139 Å) and N2-H2A…O2 (2.233 Å), connecting incoming molecule along c-axis (Figure 2a) in a zig-zag fashion. Evidently, the asymmetric molecule forms a supramolecular aggregate consists of 7 molecules in the *bc*-plane as shown in Figure 2b.

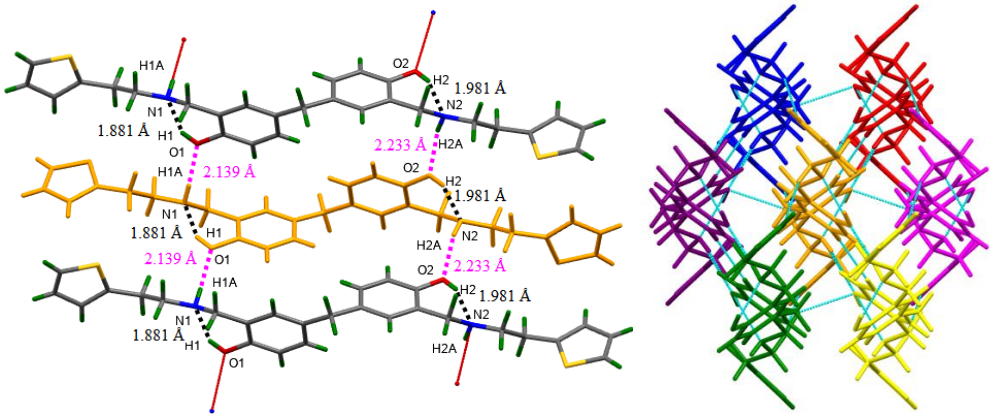

(a) (b)

Figure 2. Asymmetric molecule of **H_2L^1** forming (a) intra- and intermolecular H-bonding interactions, arranges the molecules along *c*-axis (tilted down), (b) supramolecular aggregate consists of 7 molecules in the *bc*-plane.

Notably, H-bonding interactions give 1D zig-zag arrangement of molecules along c-axis which is extend along b-axis through a number donor-acceptor C-H…$S_{thiophene}$, C-H…$O_{phenolic}$ intermolecular contacts offered by **H_2L^1** giving an attractive 2D sheet like supramolecular structure in bc-plane as shown in Figure 3.

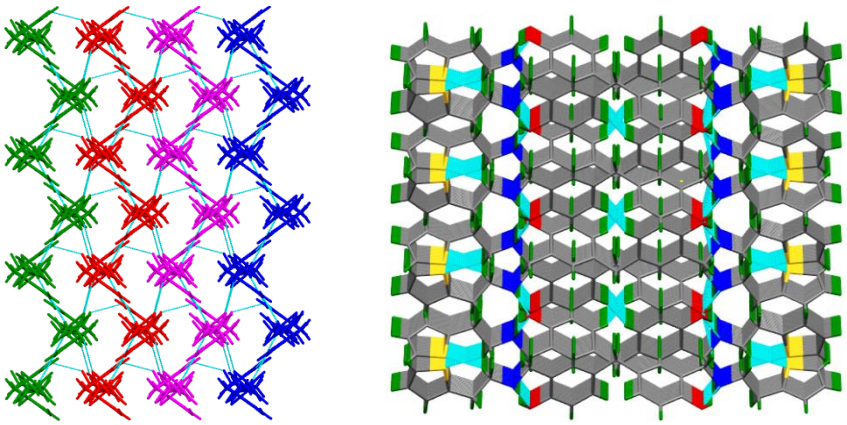

Figure 3. **(**a)View along a-axis (b) along *c*-axis (tilted down)

2.3.1.3 Density Functional Theory Calculations

Full geometry optimization of bisimines **BI-1**, **BI-2** and diamines **H_2L^1**, **H_2L^2** (Figure 4) have been performed by using density functional theory calculations at B3LYP/6-31G basis sets. All the calculations are performed using the Gaussian16 program suite and molecular orbitals were generated by GaussView 6.0 program.[28] Frontier molecular orbitals and molecular electrostatic potentials (MESP) study were discovered to be useful in predicting molecular properties and establishing structure-activity relationships.

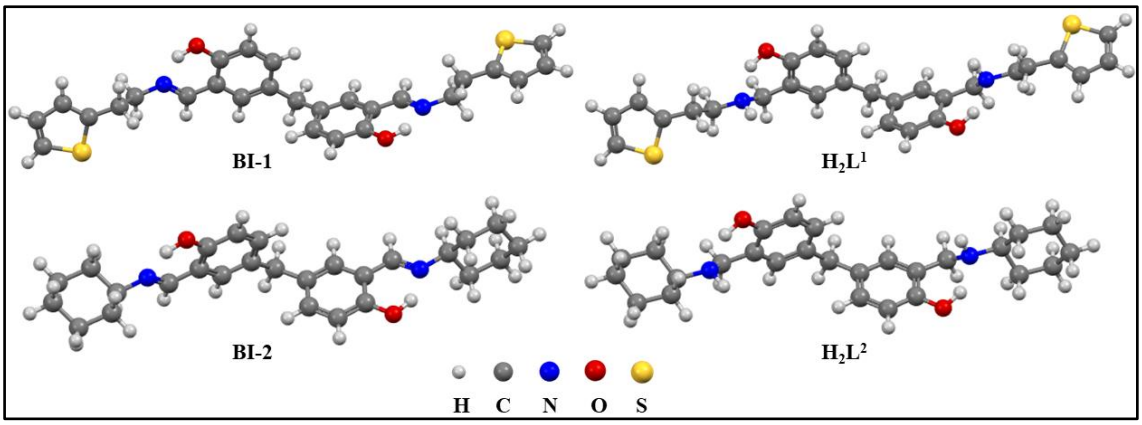

Figure 4. Optimized geometry of the molecules of **BI-1**, **BI-2**, **H_2L^1** and **H_2L^2** at B3LYP/6-31G.

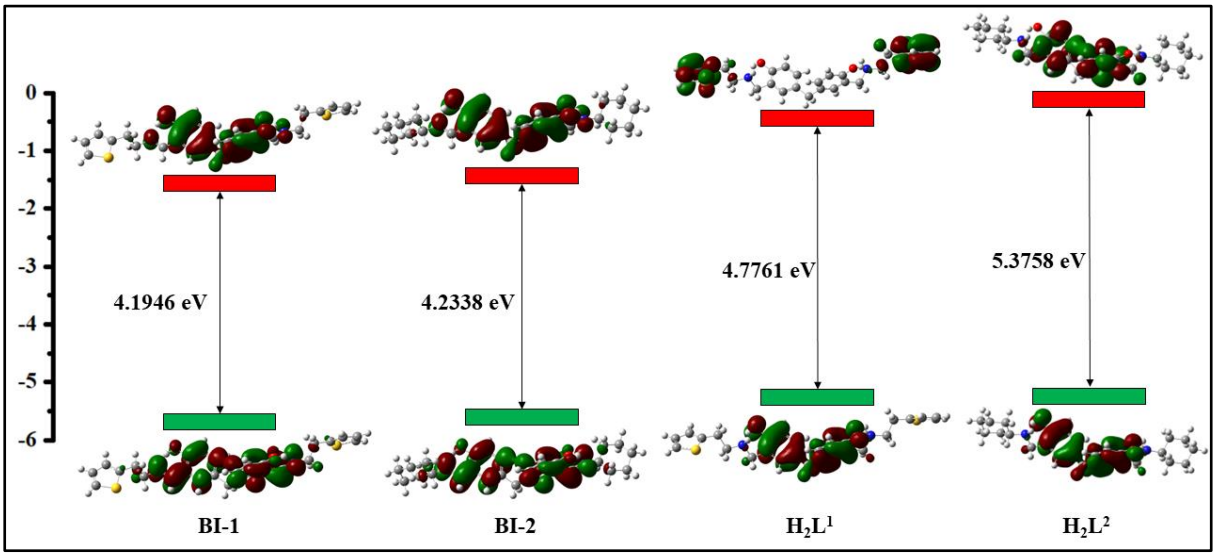

Figure 5. Analysis of frontier molecular orbitals (Isovalue= 0.02) of the compounds.

Notably, the highest occupied molecular orbitals (HOMO) are dispersed around phenyl ring of diphenylmethane whereas lowest unoccupied molecular orbitals (LUMO) are predominantly localized on diphenylmethane in all the compounds, except, H_2L^1. In H_2L^1, the lowest unoccupied molecular orbitals located on peripheral thiophene ring. The difference in the energy levels of HOMO-LUMO falls in the range of 4.194-5.375 eV (Figure 5, Table 5), suggestive of non-conducting nature of these compounds.

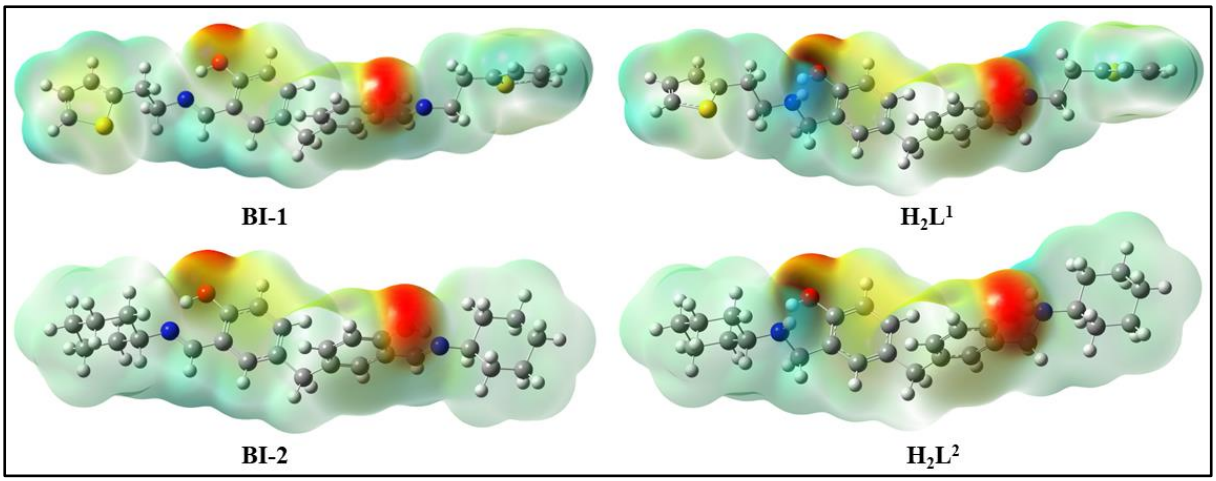

Figure 6. Representations of electron density from total SCF density (Isovalue= 0.0004; mapped with ESP).

Furthermore, the mapping of the electrostatic potential surface of bisimines **BI-1**, **BI-2** and diamines **H_2L^1**, **H_2L^2** clearly shows the presence of negative potential surrounding the phenolic -OH group(Figure 6).

Table 5. Summary of Computational study performed on **BI-1, BI-2, H_2L^1** and **H_2L^2.**

Entry	Energy (Hartree)	HOMO (eV)	LUMO (eV)	Band Gap (eV)
BI-1	-2100.4337	-5.70323	-1.50860	4.1946
BI-2	-1308.9965	-5.58296	-1.34914	4.2338
H_2L^1	-2102.8423	-5.32989	-0.55375	4.7761
H_2L^2	-1311.4020	-5.21778	0.15809	5.3758

2.3.2 Chiral bisimines BI-3, BI-4 and diamines H_2L^3, H_2L^4

2.3.2.1 Synthesis and characterization

Chiral bisimines *S*,*S*-(Thiophene-2,5-diyl)bis(N-(1-phenylethyl)-methanimine) **BI-3**, *R*,*R*-(Thiophene-2,5-diyl)bis(N-(1-phenylethyl)methanimine) **BI-4** were synthesized under a mild reaction condition in >90 % yields by condensation of 2,5-thiophenedicarboxaldehyde with different chiral amine precursors (Scheme 2). These bisimines were conveniently reduced to their diamine products *S*,*S*-(Thiophene-2,5-diyl)bis(N-(1-phenylethyl) methanamine) **H_2L^3** and *R*,*R*-(Thiophene-2,5-diyl)bis(N-(1-phenylethyl)-methanamine) **H_2L^4** at room temperature with sodium triacetoxyborohydride in dichloromethane in >80 % yields. The optimized procedure used in the synthesis of these compounds is found to be superior over several methods reported in the literature.[29] Notably, Professor Andrews[30] and his coworkers have reported the formation of *N*,*N*′-(thiophene-2,5-diylbis(methylene))-bis(α-methylbenzylamine)) from aminomethylation reactions involving metal acetylide elimination,

however this reaction led to the formation of a mixture even under several attempted conditions. The microanalysis data for **BI-3**, **BI-4**, **H_2L^3** and **H_2L^4** are consistent with their compositions and confirms their purity which is corroborated by subsequent spectral study and by X-ray diffraction analysis.

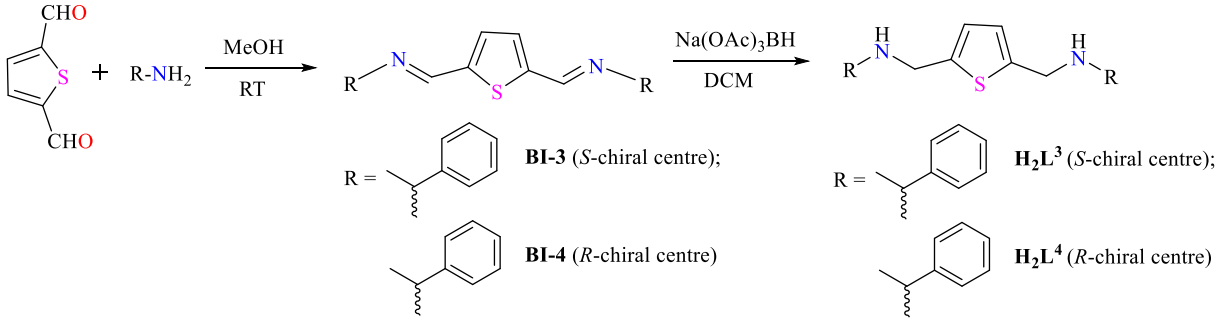

Scheme 2: Synthesis of new chiral bisimines **BI-3, BI-4** and diamines **H_2L^3, H_2L^4** holding thiophene spacers.

The ^{1}H NMR spectra of chiral bisimines **BI-3** and **BI-4** gave signals at 1.58 ppm as doublets ($J_{H\text{-}H}$ = 6.4 Hz and $J_{H\text{-}H}$ = 6.8 Hz, respectively) due to CH_3 groups coupled with CH protons at 4.52 ppm (q, $J_{H\text{-}H}$ = 6.4 Hz and $J_{H\text{-}H}$ = 6.8 Hz, respectively). Notably, CH_3 and CH groups in their reduced chiral diamines **H_2L^3** and **H_2L^4** experiences more shielding effects and appeared significantly upfield at 1.40 ppm and 3.91 ppm, respectively with the similar splitting patters. Evidently, the C*H*=N signals at 8.39 ppm in chiral bisimines **BI-3** and **BI-4** disappeared in their reduced products with an additional signal due to -N*H* and consolidates the formation of corresponding chiral diamines **H_2L^3** and **H_2L^4**. Moreover, bisimines gave all the aromatic signals as a multiplet in the expected range of 7.24-7.44 ppm whereas corresponding diamines gave thiophenyl ring protons as singlet at 6.70 ppm and phenyl ring protons as a multiplet in the range of 7.28-7.39 ppm.

The better shielding of CH_3 and CH groups in chiral diamines **H_2L^3** and **H_2L^4** is further supported by significantly upfield shifting of their ^{13}C NMR signals at 23 ppm and 45 ppm, compared to their positions in bisimines at 25 ppm and 69 ppm, respectively. The *C*H=N signals in the ^{13}C NMR spectra of bisimines are observed at 152 ppm which is expectedly missing from the similar spectra of their diamine derivatives. The IR, ^{1}H and ^{13}C NMR spectral data of these compounds are in good agreement with those closely related compounds.[29a]

A characteristic band seen in the IR spectra of chiral bisimines **BI-3** and **BI-4** is due to υ(C=N) at 1622 cm^{-1} which is expectedly missing from the similar spectra of their diamine derivatives. The chiral diamines **H_2L^3** and **H_2L^4** displayed υ(N-H) bands in the region of 3322–3329 cm^{-1}. All the compounds gave a weak intensity band in the region of 3064–2924

cm^{-1} and 2863–2820 cm^{-1} due to the aromatic υ(C-H) stretching vibrations along with a very strong band in the region of 853–820 cm^{-1} due to the aromatic υ(C-H) out-of plane bending vibrations. Apart from these bands, medium intensity bands in the regions of 1450–1452 cm^{-1} and 1350–1082 cm^{-1} are due to aromatic ring υ(C=C) and υ(C-N) stretching vibrations, respectively. Notably, all the compounds gave a medium intensity band at 761-766 cm^{-1}, attributable to C–S–C out-of-plane deformation whereas a strong band located around 700 cm^{-1}, is assignable to the out-of-plane deformation of the C–H group, a characteristic of substituted thiophene.[31]

2.3.2.2 Electronic absorption spectral study

Electronic absorption spectra (Figure 7) of all the compounds were measured at room temperature from 10^{-5} M $CHCl_3$ solution. Notably, chiral bisimines **BI-3** and **BI-4** gave a single intense electronic absorption bands primarily at 319 nm and 318 nm, respectively, attributable to n →π* (imine) transition. The imine groups attached to the thiophene in bisimines **BI-3** and **BI-4** apparently extended the π-conjugation and rigidity in the molecules and thus offers a favorable orbital overlap resulted in the photoinduced electron transfer.[32] The chiral diamines **H_2L^3** and **H_2L^4** displayed poor absorptions at 294 nm and 292 nm arises due to π →π* (phenyl) transitions. Like earlier reports,[29e] a substantial blue shifting of electronic absorption bands were observed in the reduced chiral diamines **H_2L^3** (25 nm) and **H_2L^4** (26 nm) as compared to their corresponding bisimines. However, the absorption bands in these enantiomers are not seen to be affected by the presence of diverse chirality.

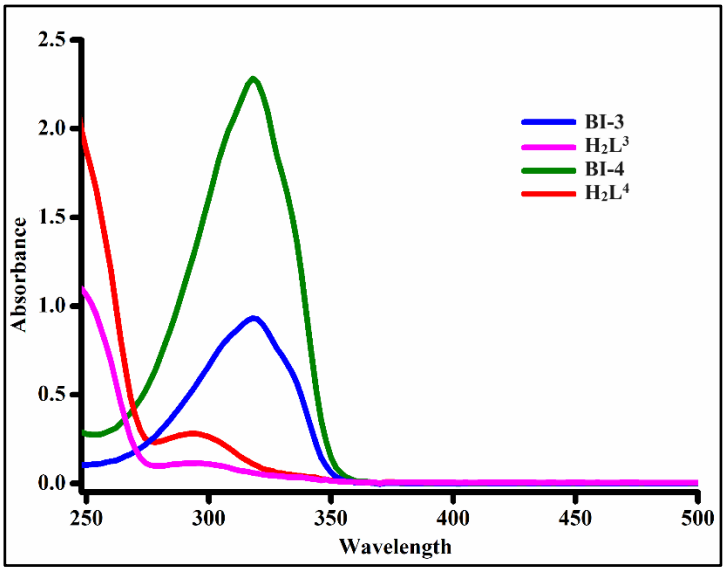

Figure 7. Electronic absorption spectra of the compounds under investigation at room temperature in 10^{-5} M $CHCl_3$.

2.3.2.3 X-ray Crystallographic Study

The single crystals of chiral bisimines enantiomers **BI-3** and **BI-4** suitable for single crystal X-ray diffraction (SCXRD) study were grown by slow evaporation from dichloromethane solution. Both the enantiomers crystallize in the orthorhombic $P22_12_1$ space group. The X-ray crystal structures of **BI-3** and **BI-4** show half of the molecules in their asymmetric units cell and complete molecules their complete molecules are generated through symmetry operation are shown in Figure 8. The crystallographic data and structure parameters for **BI-3** and **BI-4** are given in Table 6.

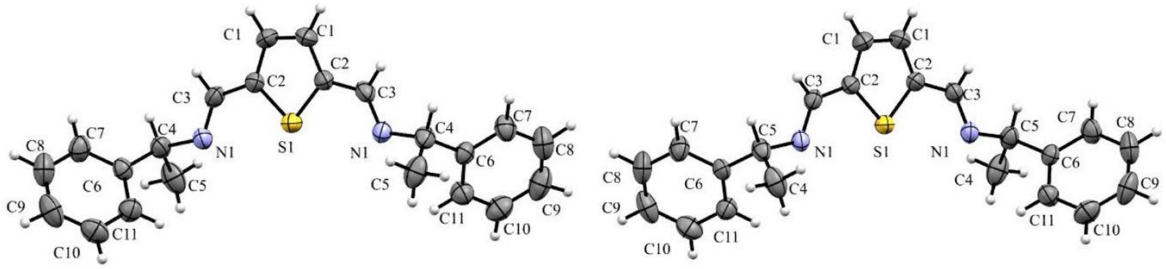

(a) **(b)**

Figure 8. X-ray structure of (a) **BI-3** and (b) **BI-4** with atom numbering scheme.

Table 6. Crystal data and structure parameters for the compounds **BI-3** and **BI-4**.

Identification Code	**BI-3**	**BI-4**
CCDC Number	2279434	2279433
Empirical formula	$C_{11}H_{11}NS_{0.5}$	$C_{11}H_{11}NS_{0.5}$
Formula weight	173.24	173.24
Temperature/K	293	293
Crystal system	orthorhombic	orthorhombic
Space group	$P22_12_1$	$P22_12_1$
a/Å	6.0702(6)	6.0660(15)
b/Å	7.7258(8)	7.716(2)
c/Å	20.706(2)	20.678(5)
α/°	90	90
β/°	90	90
γ/°	90	90
Volume/Å^3	971.03(18)	967.9(4)
Z	4	4
ρ_{calc}g/cm^3	1.185	1.196
μ/mm^{-1}	0.173	0.173
F(000)	368	372
Crystal size/mm^3	0.5 × 0.1 × 0.1	0.4 × 0.12 × 0.1
Radiation	Mo Kα (λ = 0.71073)	Mo Kα (λ = 0.71073)
2Θ range for data collection/°	6.58 to 57.84	6.58 to 52.72
Index ranges	-7 ≤ h ≤ 8, -10 ≤ k ≤ 10, -27 ≤ l ≤ 27	-7 ≤ h ≤ 7, -9 ≤ k ≤ 9, -25 ≤ l ≤ 24

Reflections collected	6732	5709
Independent reflections	2261 [R_{int} = 0.0710, R_{sigma} = 0.0915]	1960 [R_{int} = 0.0445, R_{sigma} = 0.0440]
Data/restraints/parameters	2261/0/158	1960/0/115
Goodness-of-fit on F^2	1.033	1.008
Final R indexes [I>=2σ (I)]	R_1 = 0.0543, wR_2 = 0.0695	R_1 = 0.0385, wR_2 = 0.0877
Final R indexes [all data]	R_1 = 0.1061, wR_2 = 0.0878	R_1 = 0.0456, wR_2 = 0.0911
Largest diff. peak/hole / e $Å^{-3}$	0.24/-0.32	0.17/-0.30
Flack parameter	0.09(13)	-0.02(10)

To reinforce the experimental outcomes, the geometry of all the molecules have been optimized by density functional theory calculations. A careful comparison of selected structural parameters reveals that calculated bond lengths in **BI-3** viz. $S_{thiophene}$-$C_{thiophene}$ = 1.8154 Å, C_{imine}-N_{imine} = 1.2889 Å and C_{chiral}-C_{methyl} = 1.5416 Å are significantly overestimated, while certain parameters *ca* $C_{thiophene}$-C_{imine} = 1.4541 Å, N_{imine}-C_{chiral} =1.4884 Å and C_{chiral}-C_{phenyl} = 1.5256 Å, are comparable to the similar parameters obtained experimentally. Similarly, calculated bond lengths in **BI-4** viz. $S_{thiophene}$-$C_{thiophene}$ = 1.8101 Å, C_{imine}-N_{imine} = 1.2872 Å and C_{chiral}-C_{methyl} = 1.5457 Å are significantly overestimated, $C_{thiophene}$-C_{imine} = 1.4460 Å is underestimated while certain parameters *ca* N_{imine}-C_{chiral} =1.4736 Å and C_{chiral}-C_{phenyl} = 1.5261 Å, are comparable to the similar parameters obtained experimentally. Moreover, calculated angles are found to be consistent with the experimentally determined similar parameters, except overestimated C_{imine}-N_{imine}-C_{chiral} bond angle (119.54º) in **BI-4.** The details of comparison of experimetal bond lengths (Å) and bond angles (º) with theoretical value obtained by DFT calculations for all the compounds are given in Table 7.

Table 7. Comparision of experimetal bond lengths (Å) and bond angles (º) with theoretical value obtained by DFT calculations.

Entry	Selected Bond	Bond Length (Å)	Selected Bond	Bond angle (º)
Experimental data obtained from SCXRD (This work)				
BI-3	S1-C2	1.722	S1-C2-C3	121.0
	C2-C3	1.450(4)	C2-C3-N1	123.5(3)
	C3-N1	1.260(4)	C3-N1-C4	116.7(2)
	N1-C4	1.479(4)	N1-C4-C5	108.8(3)
	C4-C5	1.516(5)	N1-C4-C6	110.3(2)
	C5-C6	1.513(4)		
BI-4	S1-C2	1.728	S1-C2-C3	120.6
	C2-C3	1.450(3)	C2-C3-N1	123.7(2)
	C3-N1	1.265(3)	C3-N1-C5	116.9(2)
	N1-C5	1.471(3)	N1-C5-C4	109.4(2)

	C4-C5	1.519(3)	N1-C5-C6	110.1(1)
	C4-C6	1.519(2)		
Theoretical data obtained from DFT (This work)				
BI-3	$S_{thiophene}$-$C_{thiophene}$	1.8154	$S_{thiophene}$-$C_{thiophene}$-C_{imine}	119.84
	$C_{thiophene}$-C_{imine}	1.4541	$C_{thiophene}$-C_{imine}-N_{imine}	120.59
	C_{imine}-N_{imine}	1.2889	C_{imine}-N_{imine}-C_{chiral}	122.28
	N_{imine}-C_{chiral}	1.4884	N_{imine}-C_{chiral}-C_{methyl}	107.17
	C_{chiral}-C_{methyl}	1.5416	N_{imine}-C_{chiral}-C_{phenyl}	116.74
	C_{chiral}-C_{phenyl}	1.5256		
BI-4	$S_{thiophene}$-$C_{thiophene}$	1.8101	$S_{thiophene}$-$C_{thiophene}$-C_{imine}	121.14
	$C_{thiophene}$-C_{imine}	1.4460	$C_{thiophene}$-C_{imine}-N_{imine}	122.85
	C_{imine}-N_{imine}	1.2872	C_{imine}-N_{imine}-C_{chiral}	119.54
	N_{imine}-C_{chiral}	1.4736	N_{imine}-C_{chiral}-C_{methyl}	108.02
	C_{chiral}-C_{methyl}	1.5457	N_{imine}-C_{chiral}-C_{phenyl}	110.30
	C_{chiral}-C_{phenyl}	1.5261		
H_2L^3	$S_{thiophene}$-$C_{thiophene}$	1.8253	$S_{thiophene}$-$C_{thiophene}$-C_{CH2}	120.52
	$C_{thiophene}$-C_{CH2}	1.5088	$C_{thiophene}$-C_{CH2}-N_{amine}	116.64
	C_{CH2}-N_{amine}	1.4729	C_{CH2}-N_{amine}-C_{chiral}	118.25
	N_{amine}-C_{chiral}	1.4796	N_{amine}-C_{chiral}-C_{methyl}	110.37
	C_{chiral}-C_{methyl}	1.5433	N_{amine}-C_{chiral}-C_{phenyl}	109.12
	C_{chiral}-C_{phenyl}	1.5240		
H_2L^4	$S_{thiophene}$-$C_{thiophene}$	1.8239	$S_{thiophene}$-$C_{thiophene}$-C_{CH2}	120.58
	$C_{thiophene}$-C_{CH2}	1.5113	$C_{thiophene}$-C_{CH2}-N_{amine}	118.52
	C_{CH2}-N_{amine}	1.4644	C_{CH2}-N_{amine}-C_{chiral}	120.65
	N_{amine}-C_{chiral}	1.4733	N_{amine}-C_{chiral}-C_{methyl}	113.79
	C_{chiral}-C_{methyl}	1.5453	N_{amine}-C_{chiral}-C_{phenyl}	109.41
	C_{chiral}-C_{phenyl}	1.5388		

Notably, each peripheral phenyl groups of **BI-4** offering C-H…π (2.774 Å; Cg1 = Cg1' = C6C7C8C9C10C11) donor-acceptor contacts, connecting four molecules anti-parallelly along c-axis and forming a supramolecular aggregate of five molecules as shown in Figure 9(a). These contacts are indeed extended 2 dimensionally and forming a fascinating 2D drill screw like architecture as shown by a spacefill model along *c*-axis as shown in Figure 9(b).

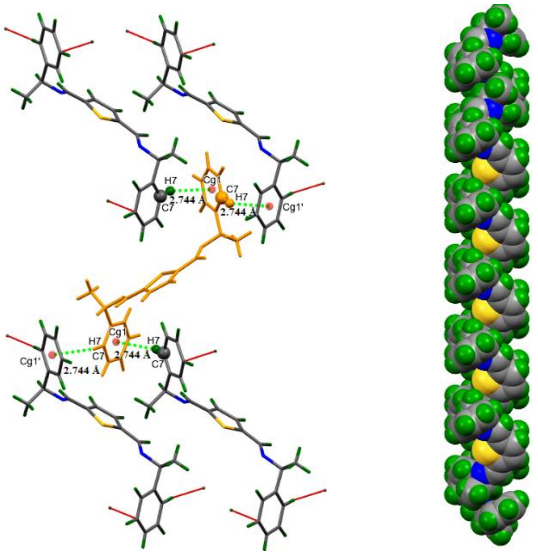

Figure 9. Molecules of **BI-4** offering C-H…π donor-acceptor contacts forming (a) supramolecular aggregate of five molecules (view along *a*-axis). (b) a fascinating 2D drill screw like architecture shown by a spacefill model along *c*-axis.

Unlike earlier reports,[33] a chirality related influence on the supramolecular packing of the enantiomer **BI-3** could not be observed and the peripheral phenyl groups are evidently involved in similar intermolecular C-H…π contacts, forming alike supramolecular assembly to that of **BI-4**. The similar packing patterns offered by both the enantiomers may be arising due to the non-involvement of chiral centres in the intermolecular contacts, however, the C-H…π (2.833 Å) donor-acceptor contacts seen in this case are found to be relatively weaker than the similar contacts in **BI-4**.

2.3.2.4 Hirshfeld surface analysis

The leading intermolecular interactions within the crystal lattice of the enantiomers **BI-3** and **BI-4** were verified by using CrystalExplorer17.[34] The two-dimensional (2D) fingerprint (FP) plots for enantiomer **BI-3** (Figure 10) and **BI-4** (Figure 12) were used for the identification of the nature of intermolecular contacts accomplished by these enantiomers in their crystal packing. These plots were further used for the relative quantification of the contacts shown in Figure 11 and Figure 13. A 2D fingerprint plot was computed for each interatomic contacts and for overall connections. The individual interatomic contacts and the reciprocal contact of each interatomic contact were considered in the computation.

The significant contribution of interatomic contacts to the crystal packing are displayed by the spikes in these plots (Figure 11 and Figure 13). In these plots, the distance from the

Hirshfeld surfaces (HS) to the nearest nucleus inside the Hirshfeld surfaces is described by *di* whereas *de* describes the distance from the HS to the nearest nucleus outside the HS. The sharp donors and acceptor spikes in these plots represent a significant interatomic contact between the protons on carbon and the centroid of peripheral phenyl rings in the crystal packing. In the crystalline lattice, the centroid of peripheral phenyl rings acting as an acceptor for weak C–H donors in **BI-3** (Figure 10) and **BI-4** (Figure 12). The existence of these intermolecular short contacts are indicated by the spikes. The H…H interactions on the Hirshfeld surfaces gave impression as the largest region of the fingerprint plot in both the enantiomers. The relative contributions of the intermolecular interactions to the Hirshfeld surface for the enantiomers **BI-3** and **BI-4** are provided in Figure 11 and Figure 13, respectively. The enantiomers **BI-3** displays; H/H (53.0 %), H/C (32.0 %), H/S (8.2 %), H/N (6.8 %) weak interactions and the enantiomers **BI-4** displays; H/H (53.3 %), H/C (31.9 %), H/S (8.2 %), H/N (6.6 %) weak interactions. Thus, we could not observe any significant difference in the relative contributions of these contacts in the packing of enantiomer **BI-3** and **BI-4**.

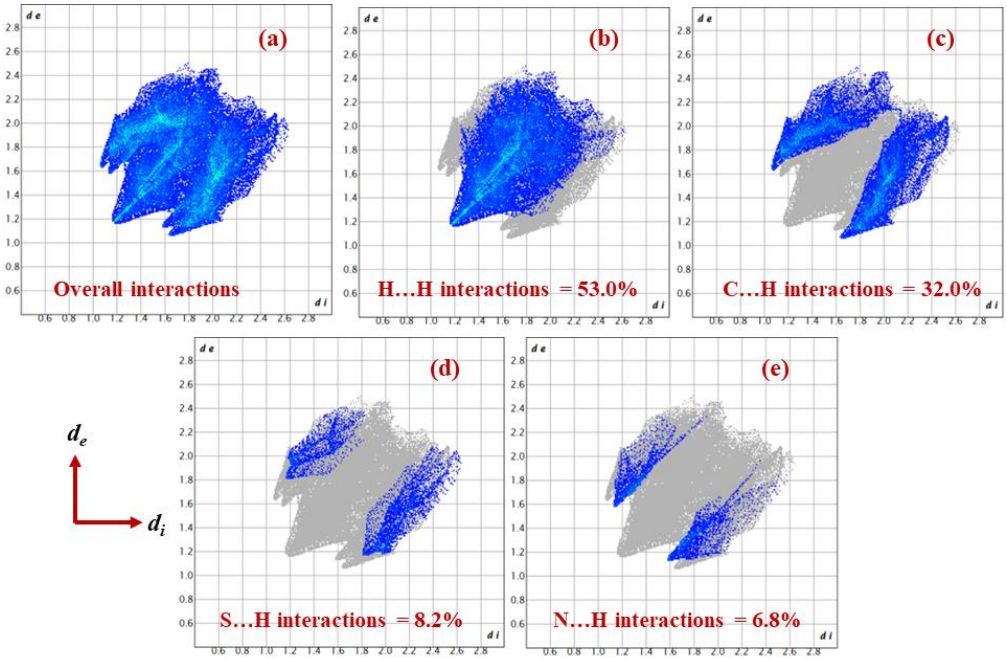

Figure 10. Decomposed Hirshfeld fingerprint plots of enantiomer **BI-3** showing the contributions of atoms within specific interacting pairs (blue areas). Specific contacts are highlighted, while the entire 2D fingerprint is shown in grey.

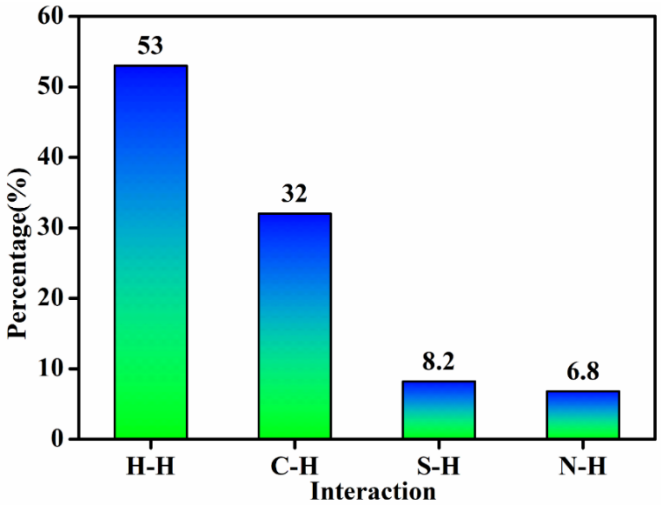

Figure 11. Relative contributions of the intermolecular interactions to the Hirshfeld surface of enantiomer **BI-3** [%].

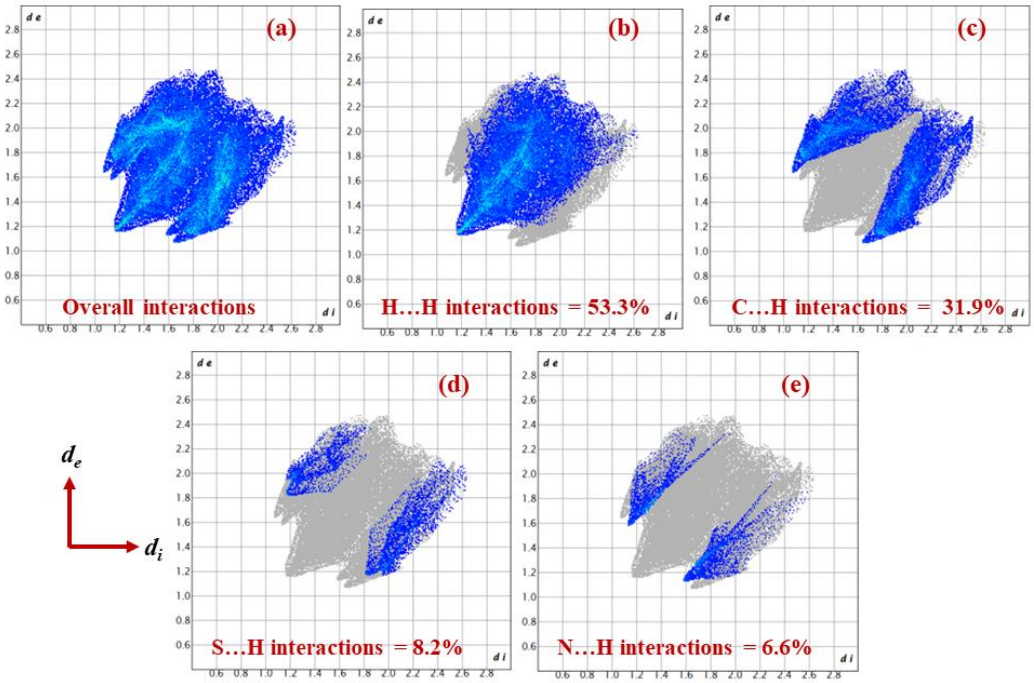

Figure 12. Decomposed Hirshfeld fingerprint plots of enantiomer **BI-4** showing the contributions of atoms within specific interacting pairs (blue areas). Specific contacts are highlighted, while the entire 2D fingerprint is shown in grey.

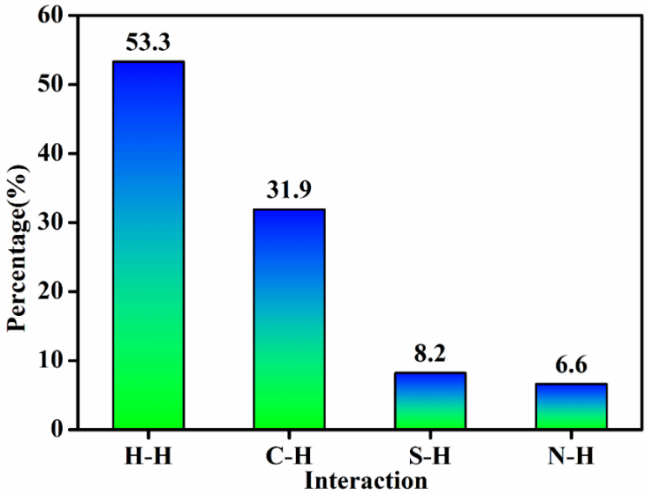

Figure 13. Relative contributions of the intermolecular interactions to the Hirshfeld surface of enantiomer **BI-4** [%].

2.3.2.5 In-silico study

2.3.2.5.1 Density Functional Theory Calculations

Full geometry optimization of chiral bisimines **BI-3**, **BI-4** and diamines **H_2L^3**, **H_2L^4** enantiomers (Figure 14) have been executed by using density functional theory calculations at B3LYP/6-31G basis sets. All the calculations are performed using the Gaussian16 program suite and molecular orbitals were generated by GaussView 6.0 program.[28]

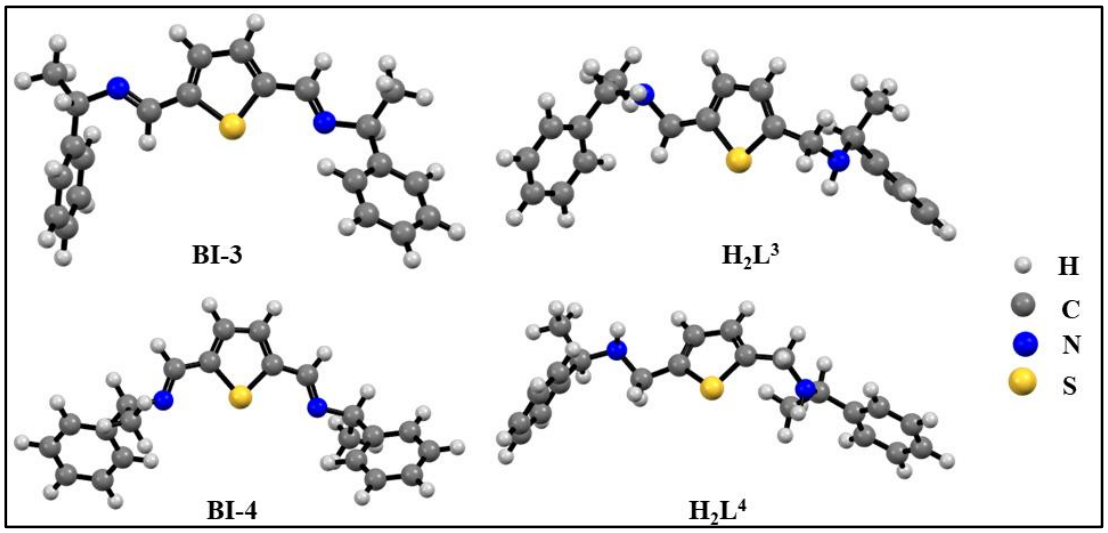

Figure 14. Optimized geometry of the molecules of **BI-3**, **BI-4**, **H_2L^3** and **H_2L^4** at B3LYP/6-31G.

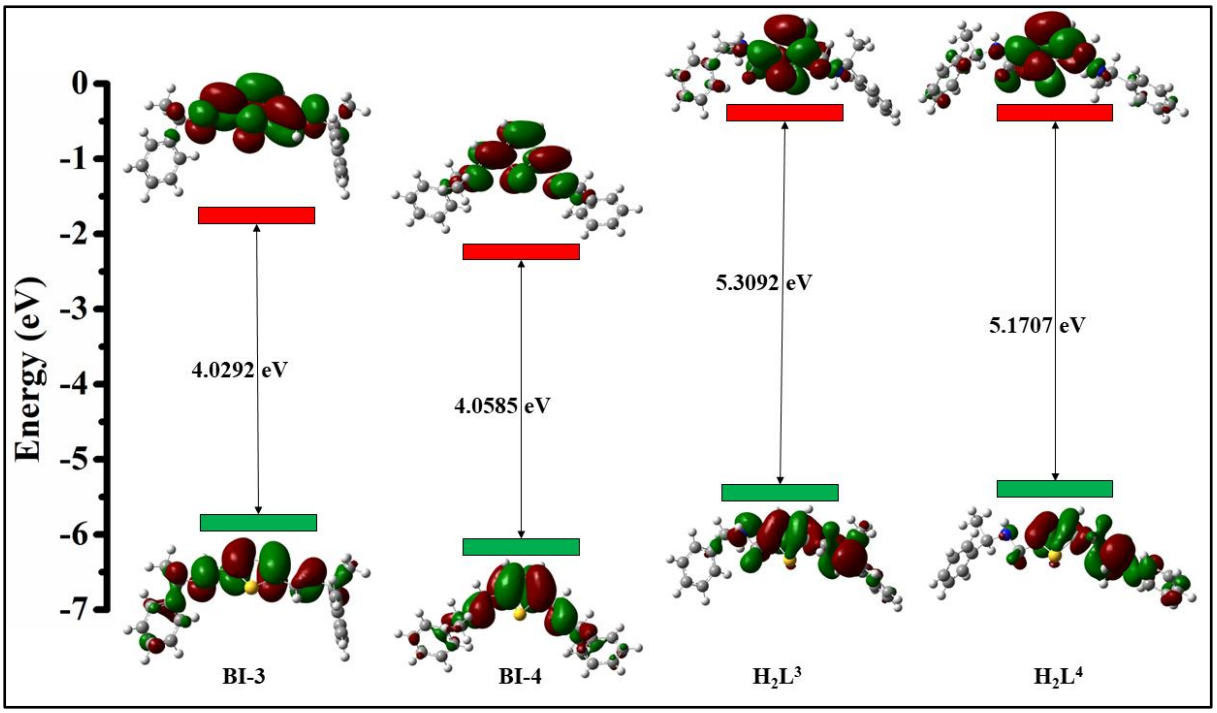

Figure 15. Analysis of frontier molecular orbitals (Isovalue= 0.02) of the compounds.

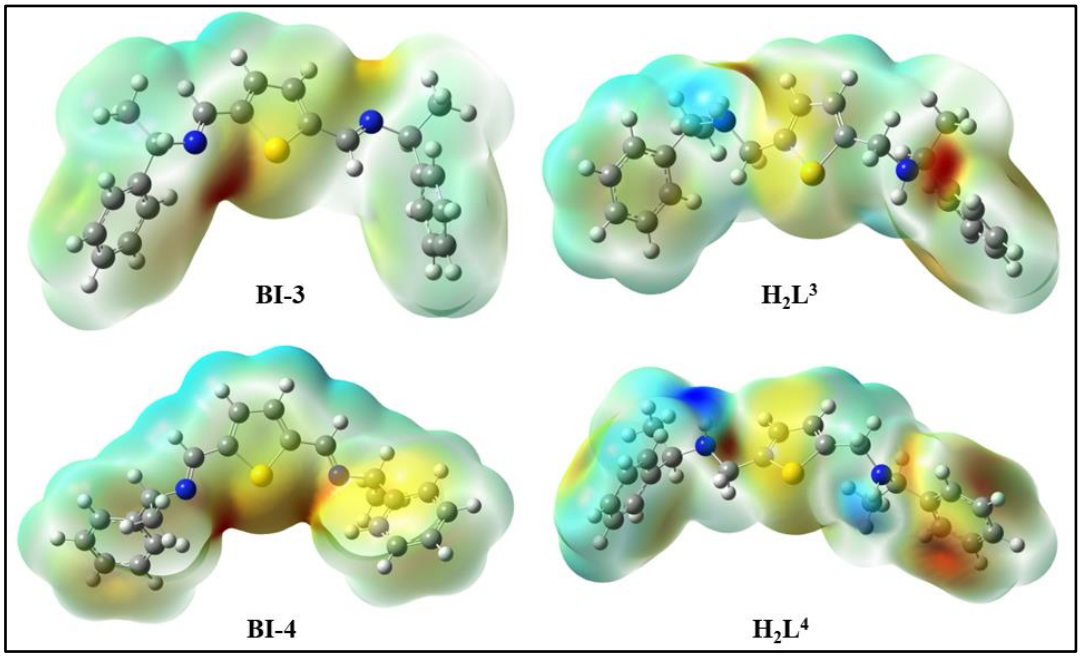

Figure 16. Representations of electron density from total SCF density (Isovalue= 0.0004; mapped with ESP).

Notably, the highest occupied molecular orbitals (HOMO) are spread over central thiophene and peripheral phenyl rings whereas lowest unoccupied molecular orbitals (LUMO) are predominantly localized over thiophene in all the compounds. The difference in the energy levels of HOMO-LUMO falls in the range of 4.029-5.309 eV (Figure 15, Table 8), suggestive

of non-conducting nature of these enantiomers. Moreover, the occurrence of negative potential around one of the peripheral phenyl rings and positive potential around other peripheral phenyl rings can be clearly visualized in the mapping of electrostatic potential surface of bisimines **BI-3**, **BI-4** and diamines **H_2L^3**, **H_2L^4** (Figure 16; Red and blue colour symbolizes localization of negative and positive potential respectively). This apparently facilitate C-H…π donor-acceptor contacts involving these groups, leading to 2D supramolecular assembly in the solid state (*vide supra*). The molecular electrostatic potential (MESP) of a drug molecule would be a convincing factor for determining their properties and potentials to facilitate the interactions with biomolecules required to observe improved bio-activity.[35]

Table 8. Summary of Computational study performed on **BI-3, BI-4, H_2L^3** and **H_2L^4.**

Entry	Energy (Hartree)	HOMO (eV)	LUMO (eV)	Band Gap (eV)
BI-3	-1358.974747	-5.9658	-1.9366	4.0292
BI-4	-1358.984075	-6.1378	-2.0792	4.0585
H_2L^3	-1361.396143	-5.6518	-0.3426	5.3092
H_2L^4	-1361.396013	-5.5470	-0.3763	5.1707

2.3.2.5.2 Ligand-protein interactions

We have selected tumor necrosis factor alpha (TNF-α) protein to perform virtual screening of newly synthesized enantiomers for their potential biological utility via a ligand-protein binding study. The selected protein is a pleiotropic pro-inflammatory cytokine act as central biological regulator in critical immune functions, however its abnormality is linked with a number of diseases. Reports suggest that inhibition of TNF-α has considerable therapeutic potential for diseases such as cancer, diabetes, and especially autoimmune diseases.[36] Researchers have been taking due interest to perform virtual screening of small molecules *via* molecular docking study before undertaking biological *in-vitro* cell assay study.[36, 37] Based on TNF-α inhibition activity, certain compounds have showed profound inhibitory activity in low micro molar concentration. Several parameters such as pharmacophore matching, interacting residues, docking score, more affinity towards TNF-α with diverse scaffolds are being used to select certain compounds for in vitro activity study.

Thus, the identification of small molecules that can inhibit TNF-α regulated pathway presents a promising and current focus area. Drugs reported till to date are proteins or antibodies, with higher molecular weight and are associated with various side effects *viz.* tuberculosis, congestive heart failure, lupus, demyelinating disease, injection site reaction, production of

auto-antibodies and systematic side effects.[38] However, the interactions of TNF-α receptors with small molecules are far less studied.[39, 40] In the present study, an integrated virtual screening approach is employed to explore new TNF-α inhibitors (PDB ID: 1TNF and 2AZ5) protein. The docking study on both the proteins showed complementary H-bonding and hydrophobic interaction with active sites of the protein (Figure 17), except **H_2L^3** which offers mainly hydrogen bonding interaction with 1tnf protein. The binding energy for each inhibitor with different poses has been embodied in Table 9.

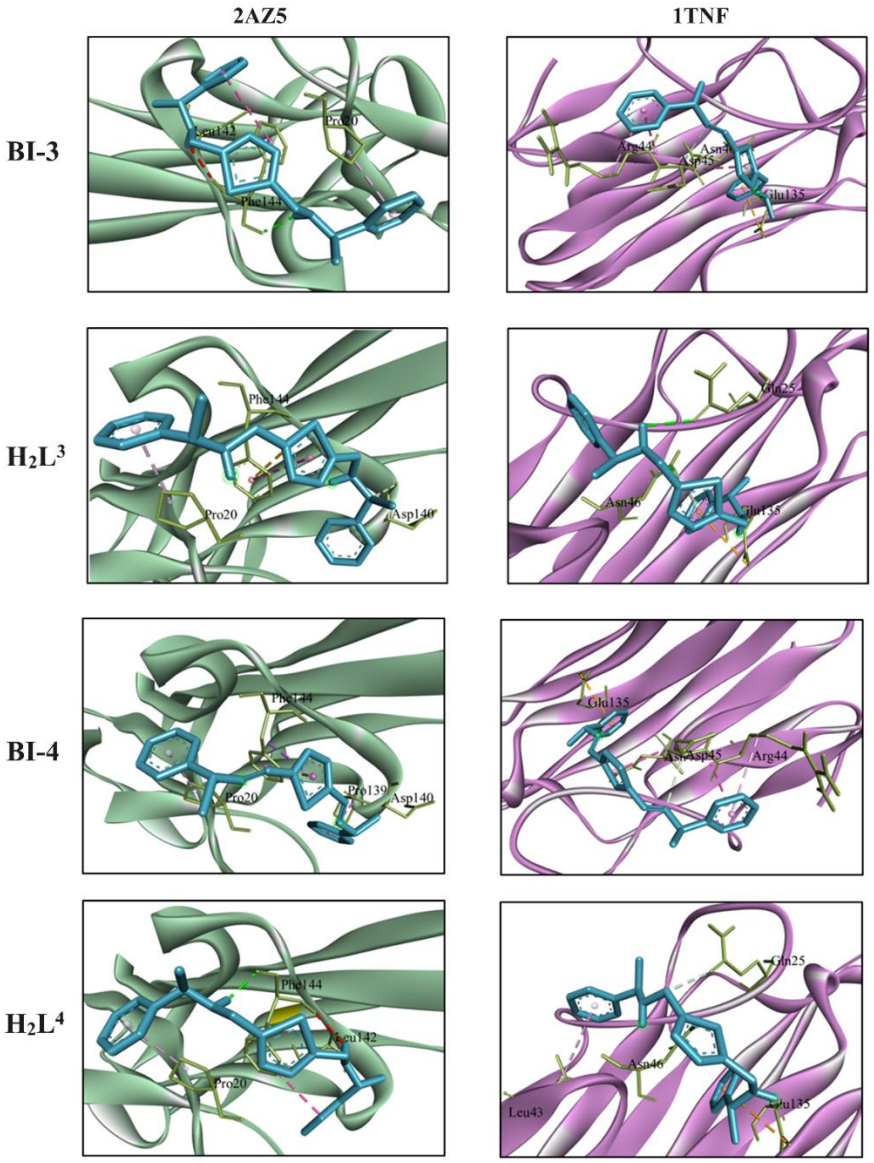

Figure 17. Binding of inhibitors **BI-3**, **BI-4**, **H_2L^3** and **H_2L^4** with TNFα receptors.

Unlike our earlier observation,[33] we could not observe measurable difference in the binding energy of enantiomers with both the proteins, expect chiral diamines enantiomers **H_2L^3** (-5.9 Kcal/mol) and **H_2L^4** (-6.1 Kcal/mol) with 1TNF protein (Table 9). Moreover, unlike **H_2L^3**,

enantiomer **H_2L^4** evidently offers a hydrophobic interaction with LEU43 site of 1TNF protein. The enantiomer **H_2L^4** displaying highest binding energy with 1TNF protein and more number of H-bonding interaction with PHE144 and LEU142 sites of 2AZ5 protein would be projected as a better drug candidate to perform further investigations.

Table 9. Interactions ligands with TNFα receptors (2AZ5 & 1TNF) within 6 Å of Active sites.

PDB Code	Compound	Ligand interaction			Binding Energy (Kcal/mol)
		Hydrogen bonding interaction	Electrostatic interaction	Hydrophobic interaction	
1TNF	**BI-3**	ASP45	GLU135	ARG44, ASP45, ASN46	-5.8
1TNF	**H_2L^3**	ASN46, GLN25	GLU135	-	-5.9
1TNF	**BI-4**	ASP45	GLU135	ARG44, ASP45, ASN46	-5.8
1TNF	**H_2L^4**	ASN46, GLN25	GLU135	LEU43	-6.1
2AZ5	**BI-3**	PHE144, LEU142	-	PHE144, PRO20	-5.6
2AZ5	**H_2L^3**	ASP140	PHE144	PHE144, PRO20	-5.4
2AZ5	**BI-4**	-	-	PHE144, PRO139, ASP140, PRO20	-5.6
2AZ5	**H_2L^4**	PHE144, LEU142	-	PHE144, PRO20	-5.4

2.3.3 Bisimines BI-5, BI-6 and diamines H_2L^5, H_2L^6

2.3.3.1 Synthesis and characterization

Secondary diamines viz. *N,N'*-bis{3-(*p*-methoxybenzylamino)propyl}piperazine (**H_2L^4**) and *N,N'*-bis{3-(p-chlorobenzylamino)propyl}piperazine (**H_2L^5**) holding *N,N'*-bispropylpiperazine linkers have been synthesized by a modified literature[25] procedures as per the following scheme.

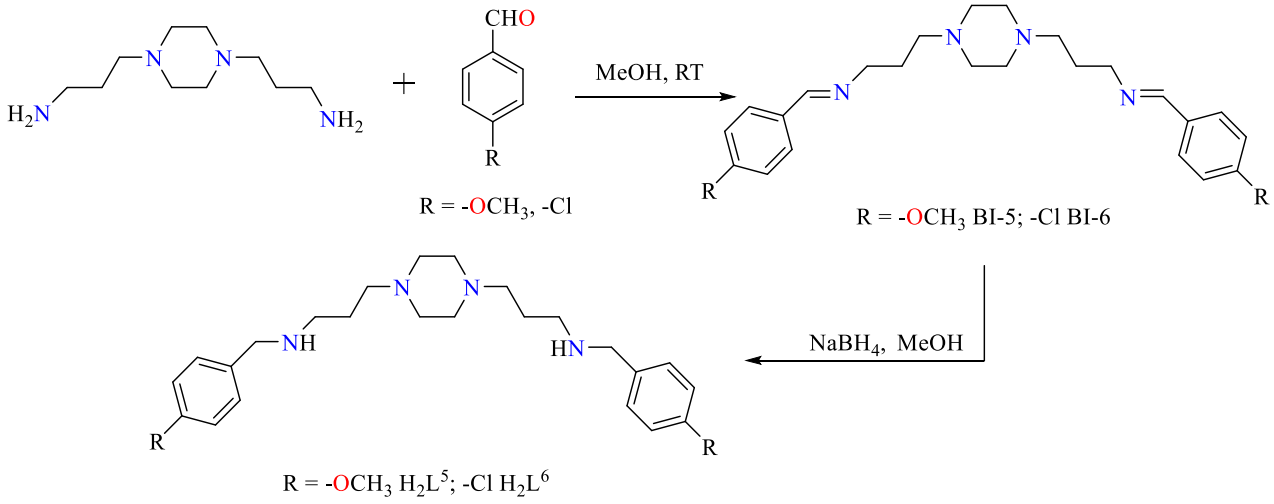

Scheme 3: Preparation of diamines holding piperazine in the linker framework.

Indeed, we have used a milder reaction condition to obtained Bisimines **BI-5, BI-6** and diamine **H_2L^5, H_2L^6** in good yield. The characterization data for **BI-5, BI-6** and diamine **H_2L^5, H_2L^6** is summarized in the experimental section and needs no further discussion. We have freshly carried out a detailed theoretical study before taking these diamine **H_2L^5, H_2L^6** for further derivatisation into their corresponding dithiocarbamate metallomacrocyclic compounds presented in Chapter 5.

2.3.3.2 Density Functional Theory Calculations

A DFT level calculation has been performed on bisimines **BI-5, BI-6** and diamines **H_2L^5, H_2L^6**. Full geometry optimization of bisimines **BI-5**, **BI-6** and diamines **H_2L^5**, **H_2L^6** (Figure 18) have been executed by using density functional theory calculations at B3LYP/6-31G basis sets. All the calculations are performed using the Gaussian16 program suite and molecular orbitals were generated by GaussView 6.0 program.[28]

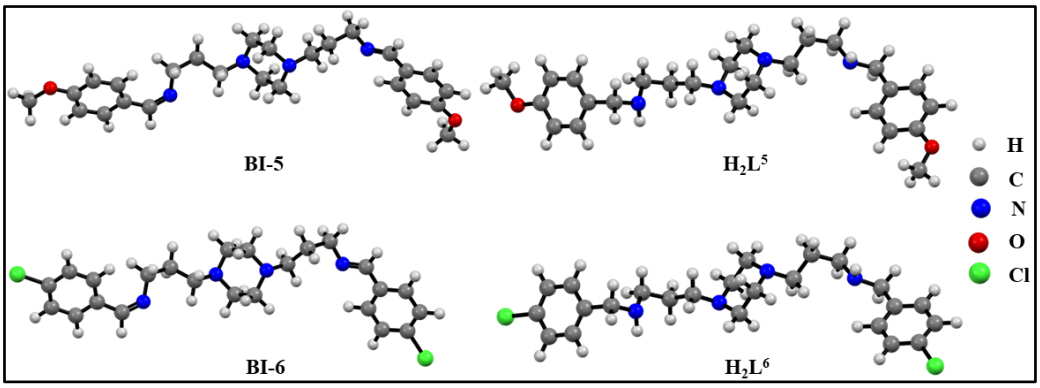

Figure 18. Optimized geometry of the molecules of **BI-5**, **BI-6**, **H_2L^5** and **H_2L^6** at B3LYP/6-31G.

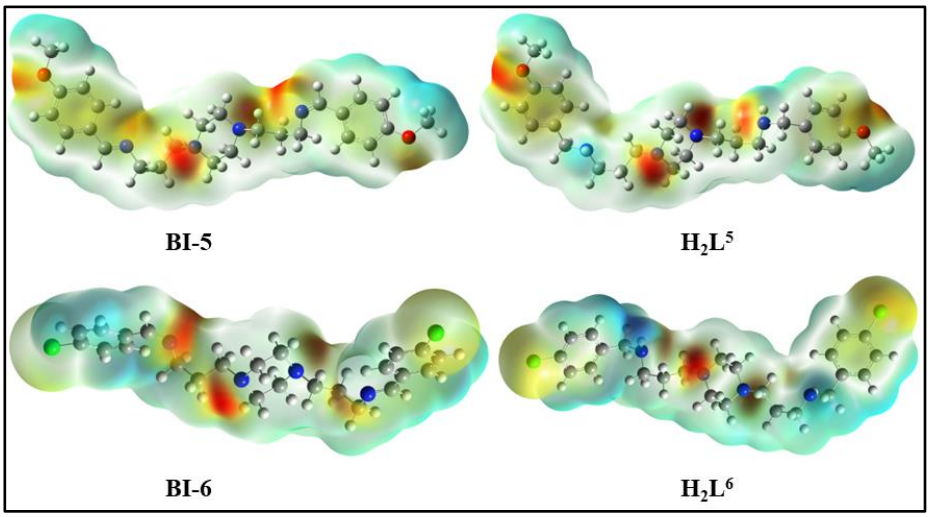

Figure 19. Representations of electron density from total SCF density (Isovalue= 0.0004; mapped with ESP).

The molecular electrostatic potential (MESP) of any chemical species gives essential information about electronic environment of molecule, which can be useful for determining its features and possible reactivity sites, including biological systems.[41] The occurrence of negative potential around one of the nitrogen of the piperazine ring in bisimines as well as diamines and slight positive potential are located at peripheral phenyl ring in the compounds (Figure 19).

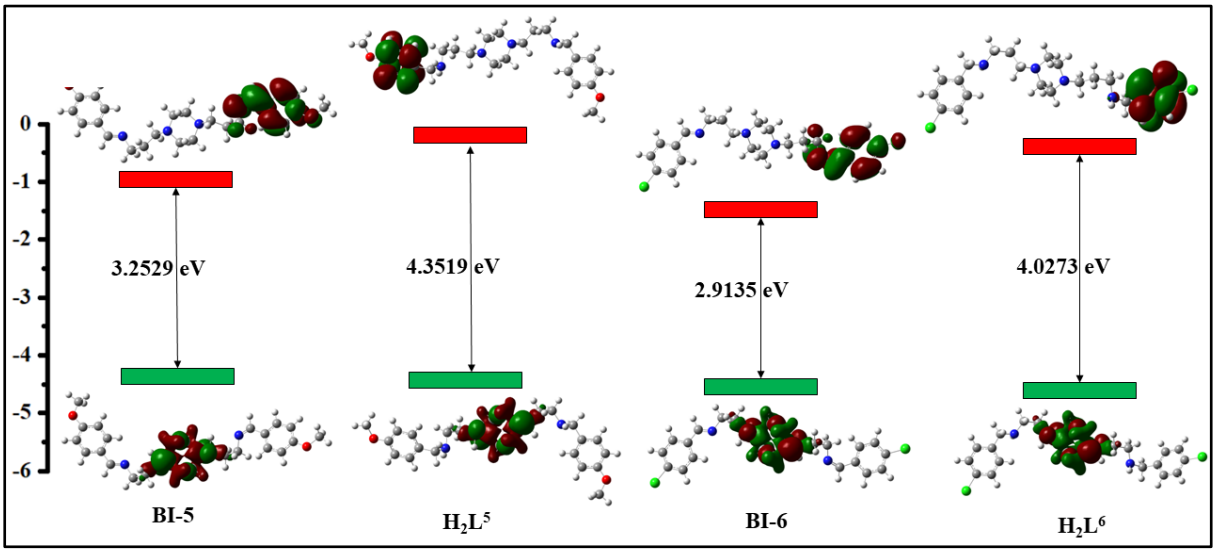

Figure 20. Analysis of frontier molecular orbitals (Isovalue= 0.02) of the compounds.

In particular, the highest occupied molecular orbitals (HOMO) are distributed over the central piperazine ring, while the lowest unoccupied molecular orbitals (LUMO) are mostly located over the peripheral phenyl ring in bisimines **BI-5, BI-6** and diamines **H_2L^5, H_2L^6**. The difference in the HOMO-LUMO energy levels suggest the band gap of these compounds. The calculated HOMO-LUMO energy gaps (Isovalue = 0.02) for bisimines **BI-5, BI-6** and diamines **H_2L^5, H_2L^6** are given in Table 10 and their localization is illustrated in Figure 20.

Table 10. Summary of Computational study performed on **BI-5, BI-6, H_2L^5** and **H_2L^6.**

Entry	Energy (Hartree)	HOMO (eV)	LUMO (eV)	Band Gap (eV)
BI-5	-1381.431827	-4.2458	-0.9929	3.2529
BI-6	-1383.857603	-4.3707	-0.0188	4.3519
H_2L^5	-2071.613435	-4.4512	-1.5377	2.9135
H_2L^6	-2074.043200	-4.5288	-0.5015	4.0273

2.4 Conclusions

In conclusion, a number of novel diamino ligand precursors such as 4,4'-methylenebis-2-((2-thiophen-2-yl)ethylamino)methylphenol (**H_2L^1**), 4,4'-methylenebis-2-(cyclohexylamino)methylphenol (**H_2L^2**), S,S-(Thiophene-2,5-diyl)bis(N-(1-phenylethyl)methanamine) (**H_2L^3**), R,R-(Thiophene-2,5-diyl)bis(N-(1-phenylethyl)methanamine) (**H_2L^4**), *N*,*N'*-bis{3-(*p*-methoxybenzylamino)propyl}piperazine (**H_2L^5**) and *N*,*N'*-bis{3-(p-chlorobenzylamino)propyl}piperazine (**H_2L^6**) holding functionalized linker framework were designed and synthesized under a mild reaction conditions. All the synthesized compounds were suitably characterized by microanalysis, ^{1}H, ^{13}C NMR, FTIR studies. The geometry of all the molecules has been optimized by using a density functional theory calculation and the theoretical data were compared well with the experimental outcomes. The non-conducting nature of these compounds are ascertained by their HOMO-LUMO band gaps falls in the range of 2.91-5.30 eV. Furthermore, a molecular docking study was employed to virtually screen these nitrogenous compounds in order to suggest possible biologically essential molecules. All diamino precursors were suitably utilized in the development of several new series of metallomacrocyclic dithiocarbamate compounds useful in in the host-guest binding study, described later in succeeding chapters.

2.5 References

[1] (a) K. Murugesan, Z. Wei, V. G. Chandrashekhar, H. Jiao, M. Beller, R. V. Jagadeesh, *Chem. Sci.* **2020**, *11*, 4332; (b) V. K. Singh, R. Kadu, H. Roy, *Eur. J. Med. Chem*. **2014**, *74*, 552; (c) C. J. Savani, H. Roy, S. K. Verma, D. R. Vennapu, V. K. Singh, *Appl. Organomet. Chem.* **2021,** *35*, e6137; (d) J. Jiang, L. Xiao, Y.-L. Li, *J. An, Synlett.* **2021**, *32*, 291.

[2] (a) M. A. Andrade, S. I. O'Donoghue, B. Rost, *J. Mol. Biol.* **1998**, *276*, 517; (b) K. A. Dill, *Biochem*. **1990**, *29*, 7133; (c) Drews, J. *Drug Discov. Today*. **2001**, *21*, 1100; (d) S. Kegnæs, J. Mielby, U. V. Mentzel, C. H. Christensen, A. Riisager, *Green Chem.* **2010**, *12*, 1437.

[3] S. D. Roughley, A. M. Jordan, *J. Med. Chem.* **2011,** *54*, 3451.

[4] T. Kimura, J. Hosokawa-Muto, Y. O. Kamatari, K. Kuwata, *Bioorg. Med. Chem. Lett*. **2011**, *21*, 1502.

[5] V. K. Singh, V. Pillai, P. Gohil, S. K. Patel, L. Buch, *J. Coord. Chem*. **2018**, *71*, 3689.

[6] (a) J. H. Kim, A. R. *Scialli, Toxicol. Sci.* **2011**, *1*, 122; (b) E. L. Izake, *J. Pharm. Sci.* **2007**, *96*, 1659.

[7] (a) C. J. Savani, D. R. Vennapu, H. Roy, V. K. Singh, *J. Organomet. Chem.* **2021,** *950*

121983; (b) C. J. Savani, R. B. Pateliya, R. R. Srivastava, D. R. Vennapu, A. K. Singh, H. Roy, D. K. Rajak, V. K. Singh, *J. Organomet. Chem.* **2023**.

[8] J. F. Vollano, S. Al-Baker, J. C. Dabrowiak, J. E. Schurig, *J. Med. Chem.* **1987**, *30*, 716.

[9] K. Zia, S. Ashraf, A. Jabeen, M. Saeed, M. Nur-e-Alam, S. Ahmed, A. J. Al-Rehaily and Z. Ul-Haq, *Sci. Rep.* **2020**, 20974.

[10] M. Feldmann, R. N. Maini, *Nat. Med.* **2003**, *9*, 1245.

[11] B. B. Aggarwal, S. C. Gupta, J. H. Kim, Blood, *J. Am. Soc. Hematol.* **2012**, *119*, 651.

[12] (a) N. Berber, A. S. Şahutoğlu, B. Gökçe, K. Çıkrıkçı, N. Gençer, *J. Mol. Struct.* **2023**, *1291*, 136061; (b) S. Kumar, P. P. Sharma, U. Shankar, D. Kumar, S. K. Joshi, L. Pena, R. Durvasula, A. Kumar, P. Kempaiah, Poonam, B. Rathi, *J. Chem. Inf. Model.* **2020**, *60*, 5754.

[13] (a) K. Das, A. Mondal, D. Pal, H. K. Srivastava, D. Srimani, *Organometallics.* **2019**, *38* 1815; (b) A. J. A. Watson, J. M. J. Williams, *Science.* **2010**, *329*, 635; (c) G. Guillena, D. J. Ramón, M. Yus, *Chem. Rev.* **2010**, *110*, 1611.

[14] (a) C. Sambiagio, S. P. Marsden, A. J. Blacker, P. C. McGowan, *Chem. Soc. Rev.* **2014**, *43*, 3525; (b) E. Sperotto, G. P. M. van Klink, G. van Koten, J. G. de Vries, *Dalton Trans.* **2010**, *39*, 10338.

[15] (a) P. Ruiz-Castillo, S. L. Buchwald, *Chem. Rev.* **2016**, *116*, 12564; (b) J. F. Hartwig, *Acc. Chem. Res.* **2008,** *41*, 1534; (c) J. Magano, J. R. Dunetz, *Chem. Rev.* **2011**, *111*, 2177.

[16] (a) D. J. van As, T. U. Connell, M. Brzozowski, A. D. Scully, A. Polyzos, *Org. Lett.* **2018**, *20*, 905; (b) R. Kadu, V. K. Singh, S. K. Verma, P. Raghavaiah, M. M. Shaikh, *J. Mol. Struct.* **2013**, *1033*, 298; (c) S. K. Verma, V. K. Singh, *J. Organomet. Chem.* **2015,** *791*, 214.

[17] (a) S. K. Patel, K. Kolte, C. J. Savani, P. Raghavaiah, D. Dave, A. A. Isab, D. Mistry, D. Suthar, V. K. Singh, *Inorganica Chim. Acta.* **2022**, *543*, 121139; (b) V. K Singh, V. Pillai, S. K. Patel, L. Buch, *ChemistrySelect.* **2019**, *4*, 8689; (c) V. Pillai, S. K. Patel, L. Buch, V. K. Singh, *Appl. Organomet. Chem.* **2018**, *32*, e4559; (d) V. Pillai, L. Buch, A. Desai, V. K. Singh, *ChemistrySelect.* **2017**, *2*, 11581; (e) R. Kadu, V. Pillai, Amrit V., V. K. Singh, *RSC Adv.* **2015**, *5*, 106688.

[18] H. Xu, Y. L. Song, L. W. Mi, H. W. Hou, M. S. Tang, Y. L. Sang, Y. T. Fan, Y. Pan, *Dalton Trans.* **2006**, 838.

[19] (a) R. Gao, D. J. Canney, *J. Org. Chem.* **2010**, *75*, 7451; (b) F. Fdhila, V. Vazquez, J. L. Sanchez, R. J. Riguera, *J. Nat. Prod.* **2003**, *66*, 1299. (c) S. Lieber, F. Scheer, W. Meissner, S. Naruhn, T. Adhikary, S. Muller-Brusselbach, W. E. Diederich, R. Müller, *J. Med. Chem.* **2012**, *55*, 2858.

[20] (a) C. B. Pollard, Jr, T. H. Wicker, *J. Am. Chem. Soc.* **1954**, *76*, 1853; (b) J. M. Salvino, B. Gerard, H. F. Ye, B. Sauvagnat, R. E. Dolle, *J. Comb. Chem.* **2003**, *5*, 260.

[21] M. S. Fonari, S. Antal, R. Castañeda, C. Ordonez, T. V. Timofeeva, *CrystEngComm.* **2016**, *18*, 6282.

[22] (a) M. K. Parai, G. Panda, K. Srivastava, S. K. Puri, *Bioorg. Med. Chem. Lett.* **2008**, *18*, 776; (b) V. K. Jain, B. Jain, U. K. Sharma, D. Saha, *J. Curr. Pharm. Res.* **2011,** *3,* 66. (c) A. Casini, A. Scozzafava, A. Mastrolorenzo, L. T. Supuran, *Curr. Cancer Drug Targets.* **2002**, *2*, 55.

[23] (a) P. Choudhary, R. Kumar, K. Verma, *Bioorg. Med. Chem*. **2006**, *14*, 1819; (b) R. S. Upadhayaya, N. Sinha, S. Jain, N. Kishore, R. Chandra, S.K. Arora, *Bioorg. Med. Chem.* **2004**, *12*, 2225; (c) S. G. Shingade, S. K. B. Bari, *Med Chem Res.* **2013**, *22*, 699.

[24] (a) J.D.E.T. Wilton-Ely, D. Solanki, G. Hogarth, *Eur. J. Inorg. Chem.* **2005**, 4027; (b) S. K. Verma, V. K. Singh, *RSC Adv*. **2015**, *5*, 53036.

[25] Sergeant, N.; Delacourte, A.; Melnyk, P.; Buee, L. US Patent (2015) Patent No.: US 9,044,478 B2.

[26] S. Forli, R. Huey, M. E. Pique, M. F. Sanner, D. S. Goodsell, A. J. Olson, *Nature Protocols.* **2016**, *11*, 905.

[27] BIOVIA, Dassault Systèmes, [Discovery Stuidos Visualiser], [2021], San Diego: Dassault Systèmes, **2021**.

[28] M. J. Frisch, G. W. Trucks, H. B. Schlegel, G. E. Scuseria, M. A. Robb, J. R. Cheeseman, G. Scalmani, V. Barone, G. A. Petersson, H. Nakatsuji, X. Li, M. Caricato, A. V. Marenich, J. Bloino, B. G. Janesko, R. Gomperts, B. Mennucci, H. P. Hratchian, J. V. Ortiz, A. F. Izmaylov, J. L. Sonnenberg, D. Williams-Young, F. Ding, F. Lipparini, F. Egidi, J. Goings, B. Peng, A. Petrone, T. Henderson, D. Ranasinghe, V. G. Zakrzewski, J. Gao, N. Rega, G. Zheng, W. Liang, M. Hada, M. Ehara, K. Toyota, R. Fukuda, J. Hasegawa, M. Ishida, T. Nakajima, Y. Honda, O. Kitao, H. Nakai, T. Vreven, K. Throssell, J. A. Montgomery, Jr, J. E. Peralta, F. Ogliaro, M. J. Bearpark, J. J. Heyd, E. N. Brothers, K. N. Kudin, V. N. Staroverov, T. A. Keith, R. Kobayashi, J. Normand, K. Raghavachari, A. P. Rendell, J. C. Burant, S. S. Iyengar, J. Tomasi, M. Cossi, J. M. Millam, M. Klene, C. Adamo, R. Cammi, J. W. Ochterski, R. L. Martin, K. Morokuma, O. Farkas, J. B. Foresman, D. J. Fox, Gaussian, Inc. Wallingford CT, **2016**.

[29] (a) V. K. Singh, R. Kadu, H. Roy, *Eur. J. Med. Chem*. **2014**, *74*, 552; (b) K. Das, A. Mondal, D. Pal, H. K. Srivastava, D. Srimani, *Organometallics*. **2019**, *38*, 1815; (c) G. Guillena, D. J. Ramón, M. Yus, *Chem. Rev*. **2010**, *110*, 1611; (d) C. Sambiagio, S. P.

Marsden, A. J. Blacker, P. C. McGowan, *Chem. Soc. Rev.* **2014**, *43*, 3525; (e) D. J. van As, T. U. Connell, M. Brzozowski, A. D. Scully, A. Polyzos, *Org. Lett.* **2018**, *20*, 905.

[30] M. T. Flynn, V. L. Blair, P. C. Andrews, *Organometallics* **2018**, *37*, 1225.

[31] (a) M. Rico, J. M. Orza, J. Morcillo, *Spectrochim. Acta*. **1965**, *21*, 689; (b) F. Alakhras, R. Holze, *Synth. Met.* **2007**, *157*, 109.

[32] H. Liu, B. Li, D. Liu, Z. Xu, *Chem. Phys. Lett.* **2001**, *350*, 441.

[33] C. J. Savani, D. R. Vennapu, H. Roy, V. K. Singh, *J. Organomet. Chem*. **2021**, *950*, 121983.

[34] M. Ashfaq, K.S. Munawar, M.N. Tahir, N. Dege, M. Yaman, S. Muhammad, S. S. Alarfaji, H. Kargar, M.U. Arshad, *ACS Omega 6* **2021**, 22357.

[35] C. J. Savani, H. Roy, S. K. Verma, D. R. Vennapu, V. K. Singh, *Appl. Organomet. Chem.* **2021**, *35*, e6137.

[36] K. Zia, S. Ashraf, A. Jabeen, M. Saeed, M. Nur-e-Alam, S. Ahmed, A. J. Al-Rehaily, Z. Ul-Haq, *Sci. Rep*. **2020**, 20974.

[37] (a) N. Berber, A. S. Şahutoğlu, B. Gökçe, K. Çıkrıkçı, N. Gençer, *J. Mol. Struct*. **2023**, *1291*, 136061; (b) S. Kumar, P. P. Sharma, U. Shankar, D. Kumar, S. K. Joshi, L. Pena, R. Durvasula, A. Kumar, P. Kempaiah, Poonam, B. Rathi, *J. Chem. Inf. Model*. **2020**, *60*, 5754.

[38] N. Scheinfeld, *J. Dermatolog. Treat*. **2004**, *15*, 280.

[39] A. Guirado, J. I. L. Sánchez, A. J. Ruiz-Alcaraz, D. Bautista, J. Gálvez, *Eur. J. Med. Chem*. **2012**, *54*, 87.

[40] M. M. He, *et al*. *Science* **2005**, *310*, 1022.

[41] (a) S. R. Gadre, P. K. Bhadane, *Resonance*, **1999**, *4*, 11. (b) F. A. Bulat, A. T.-Labbé, T. Brinck, J. S. Murray, P. Politzer, *J Mol Model* **2010**, *16*, 1679. (c) P. Politzer, P. R. Laurence, K. Jayasuriya, *Environ. Health Perspect*. **1985**, *61*, 191.

2.6 Annexures

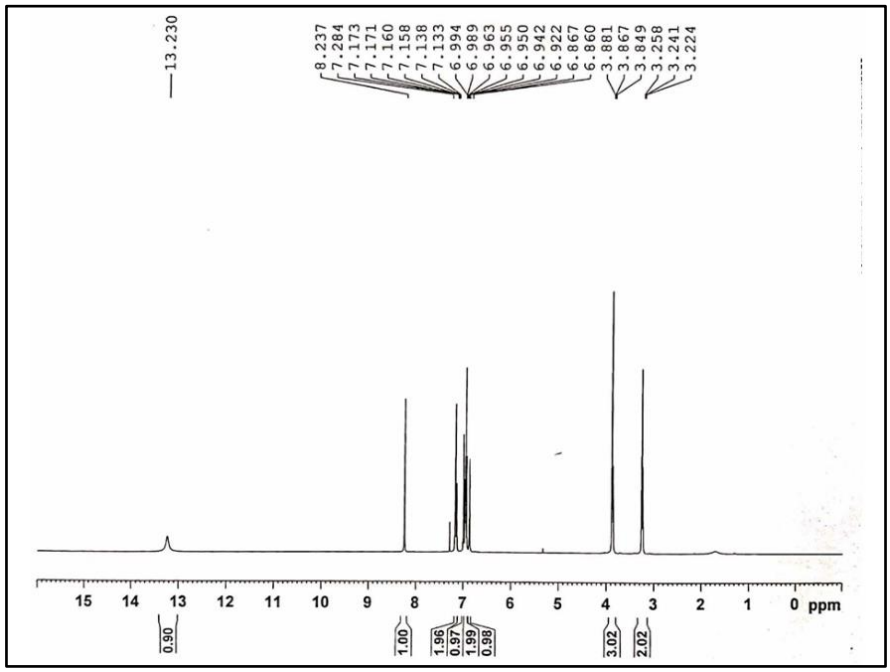

Annexure 1. ^{1}H NMR spectrum of **BI-1**.

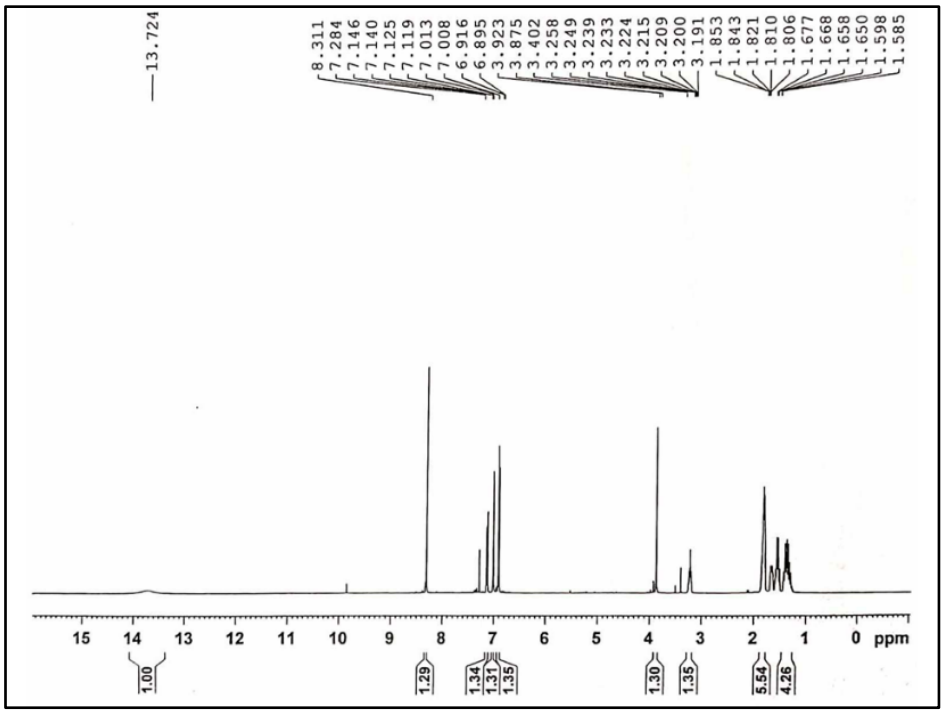

Annexure 2. ^{1}H NMR spectrum of **BI-2**.

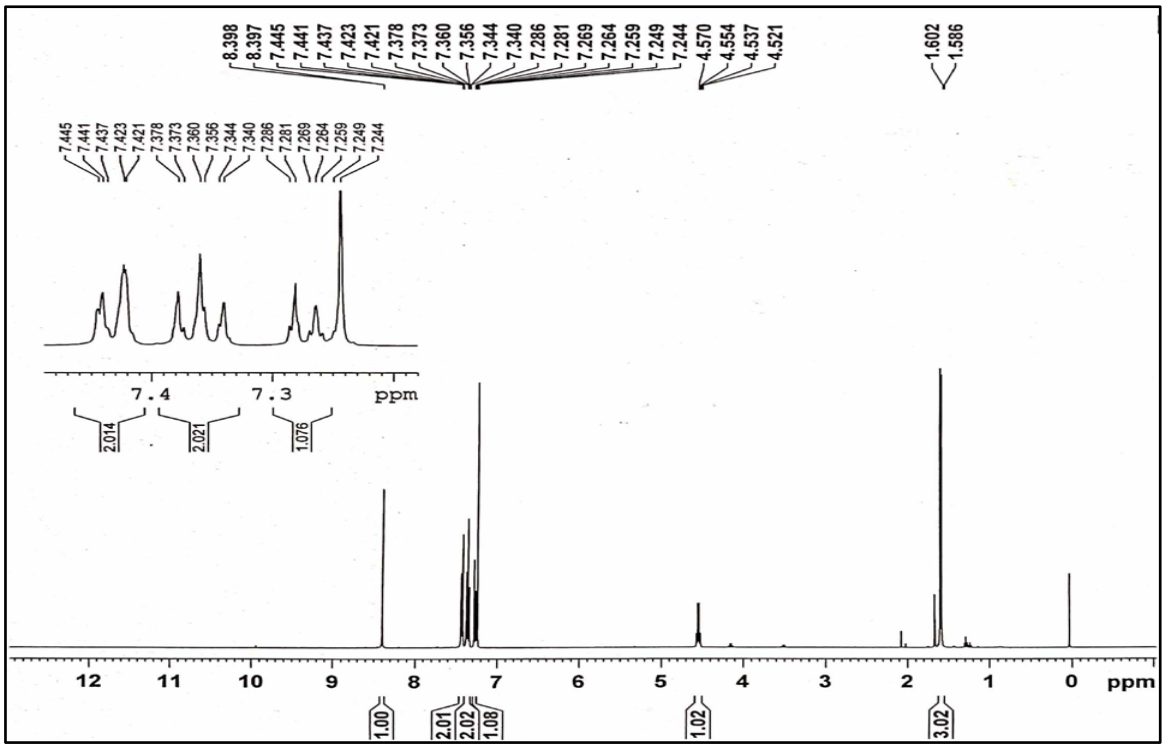

Annexure 3. ^{1}H NMR spectrum of **BI-3**.

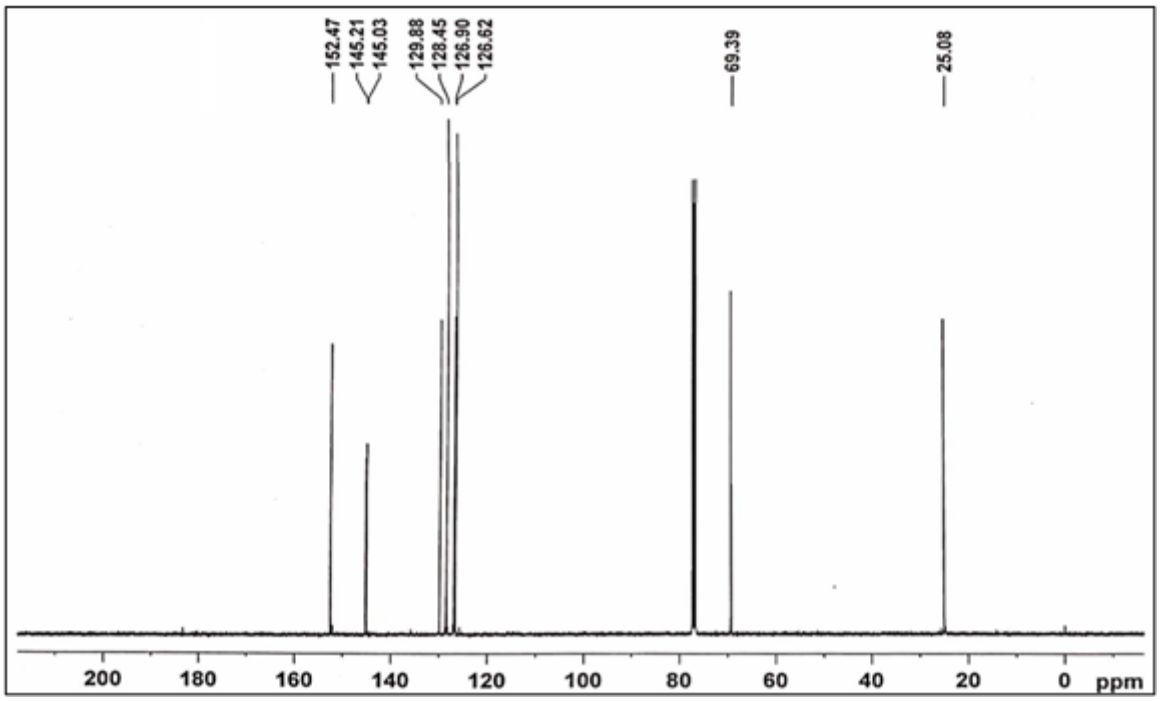

Annexure 4. ^{13}C NMR spectrum of **BI-3.**

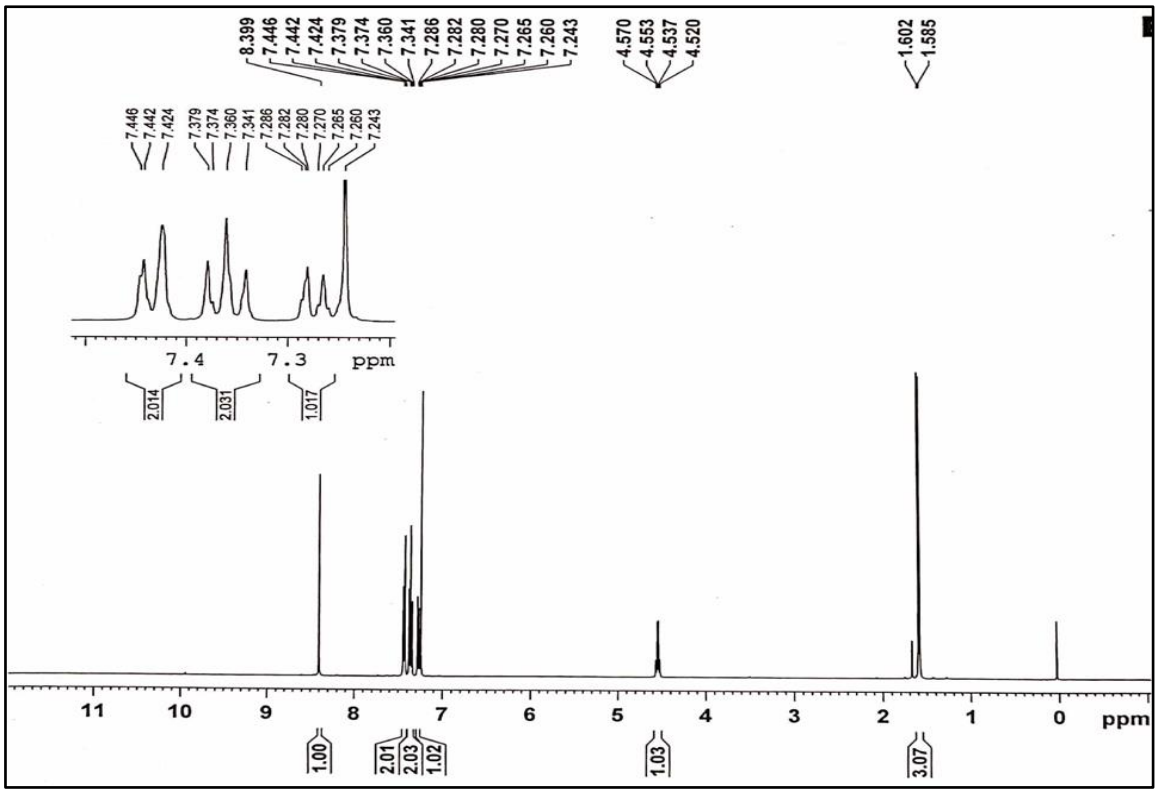

Annexure 5. ^{1}H NMR spectrum of **BI-4**.

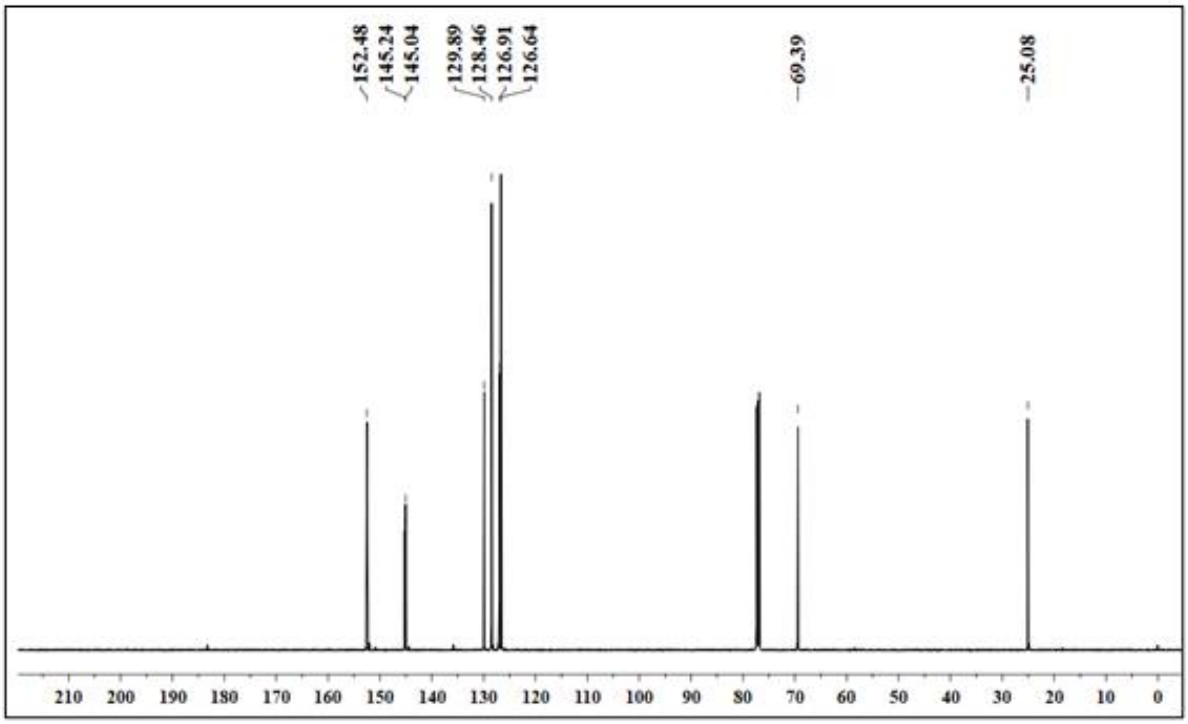

Annexure 6. ^{13}C NMR spectrum of **BI-4.**

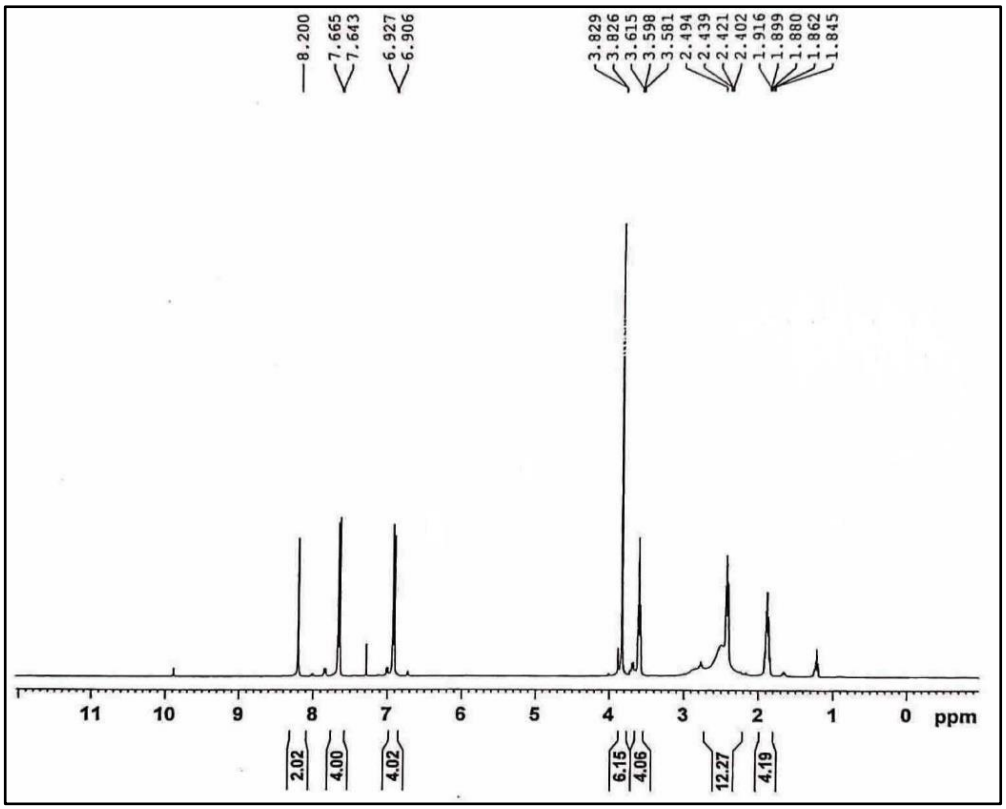

Annexure 7. ^{1}H NMR spectrum of **BI-5**.

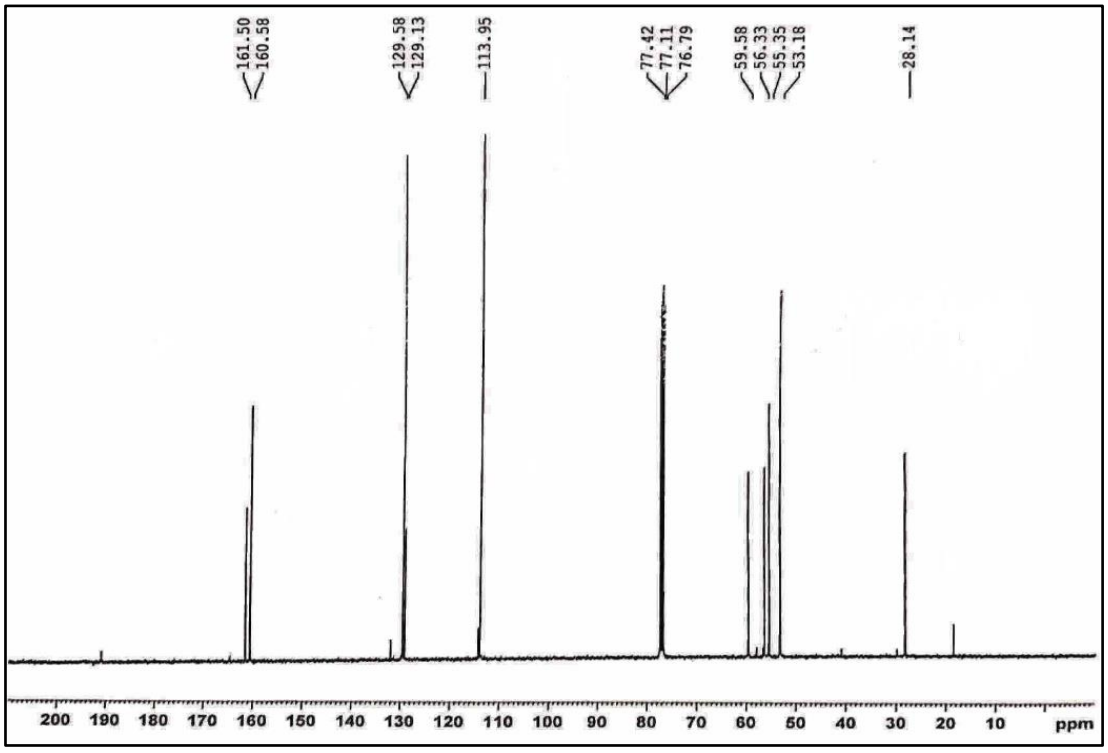

Annexure 8. ^{13}C NMR spectrum of **BI-5.**

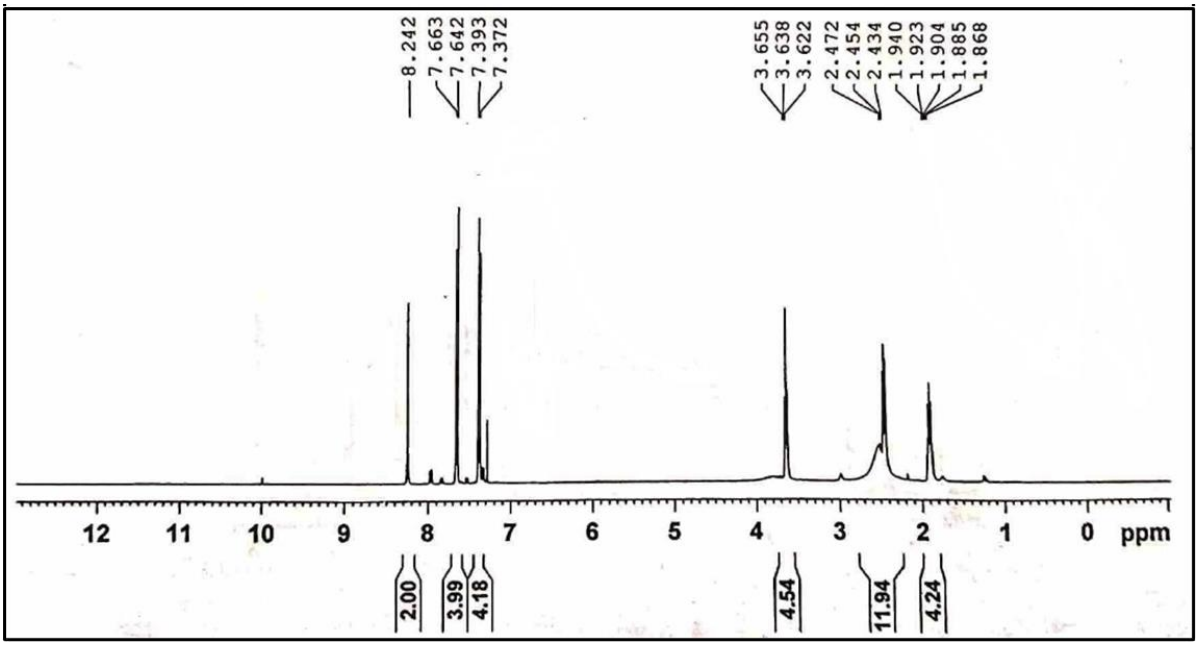

Annexure 9. ^{1}H NMR spectrum of **BI-6**.

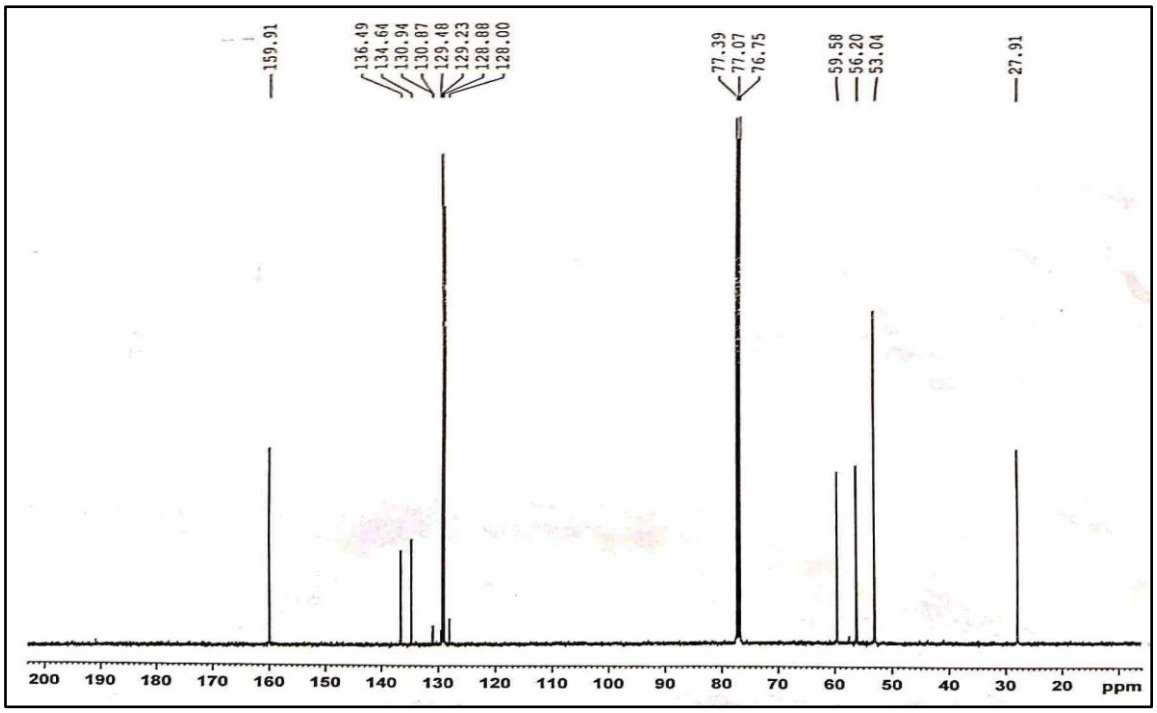

Annexure 10. ^{13}C NMR spectrum of **BI-6.**

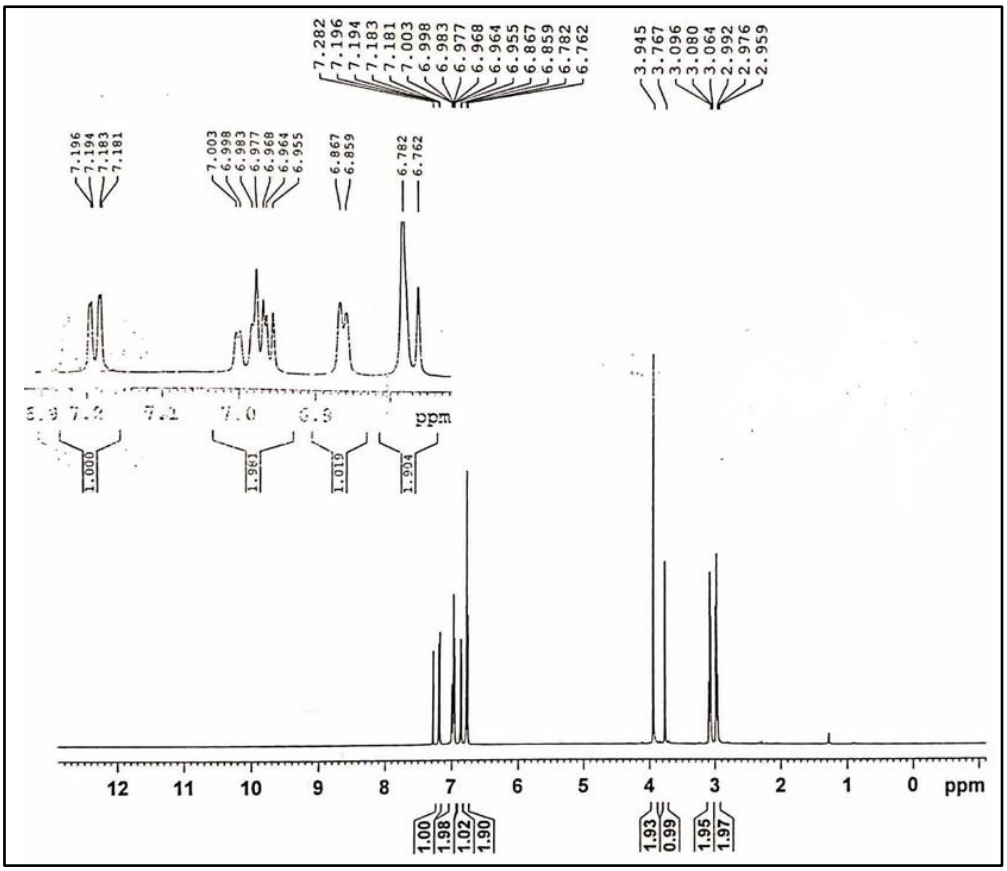

Annexure 11. ^{1}H NMR spectrum of **H_2L^1**.

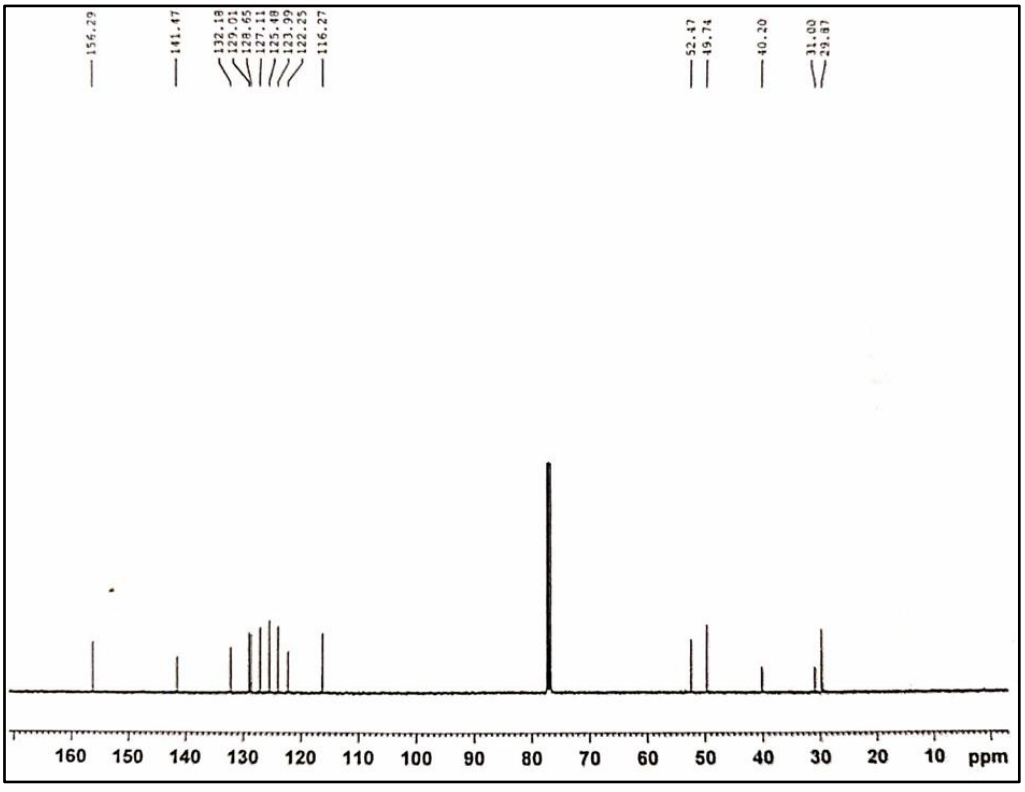

Annexure 12. ^{13}C NMR spectrum of **H_2L^1**.

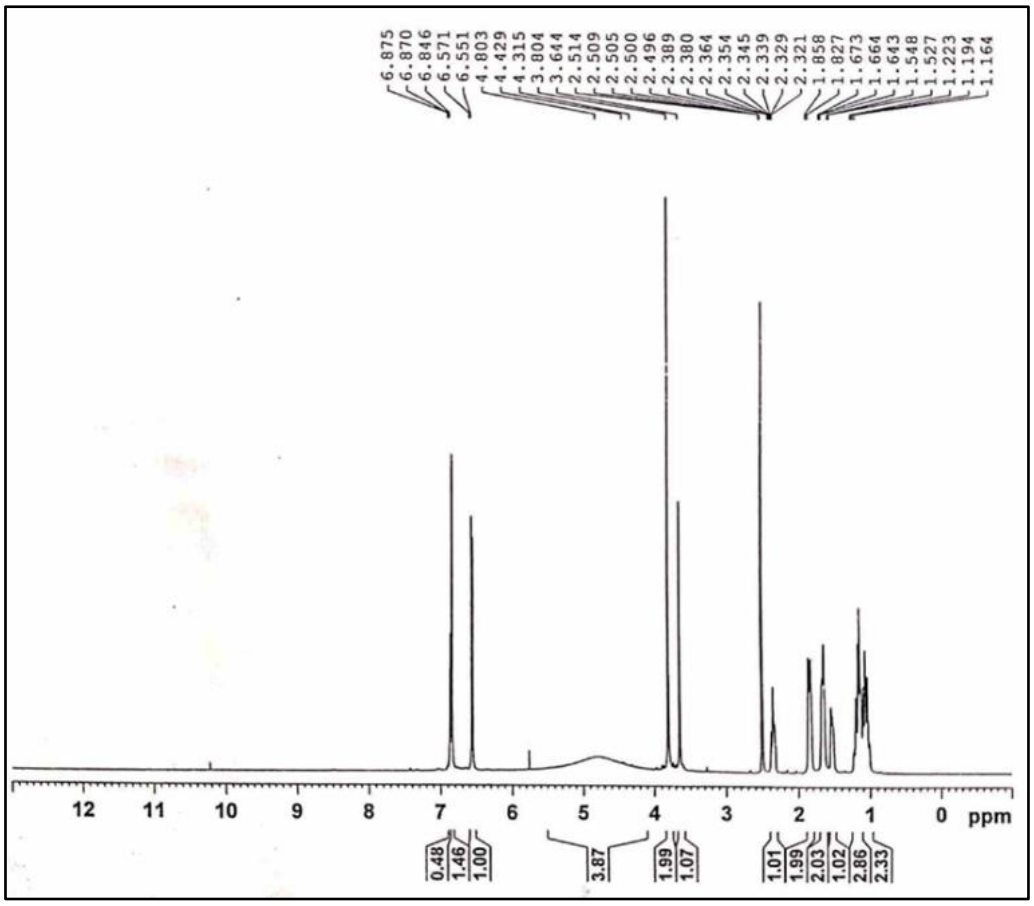

Annexure 13. ^{1}H NMR spectrum of **H_2L^2**.

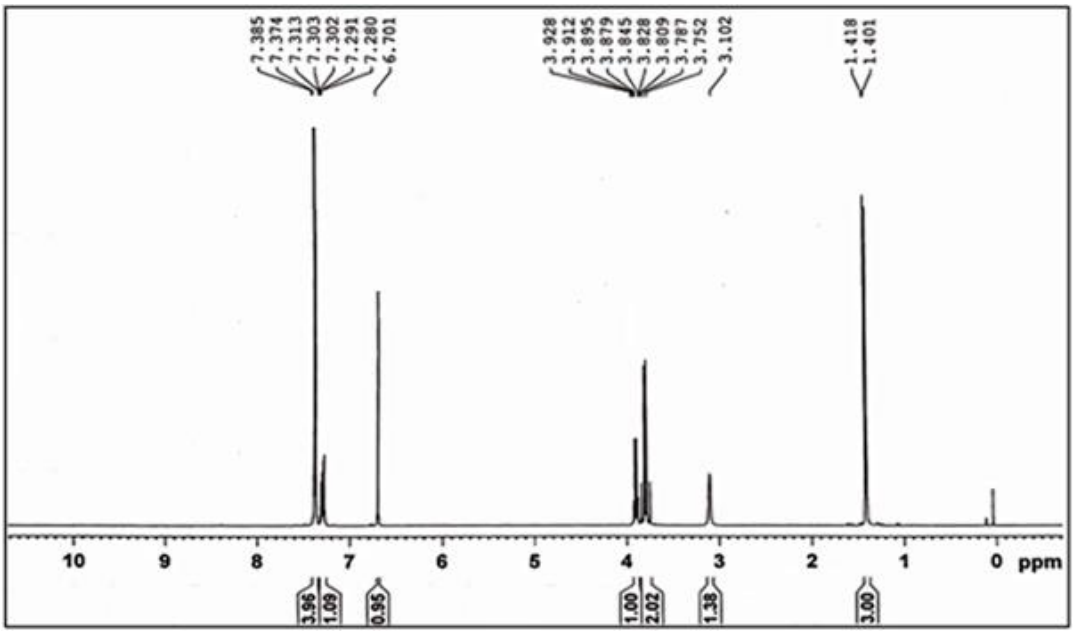

Annexure 14. ^{1}H NMR spectrum of **H_2L^3**.

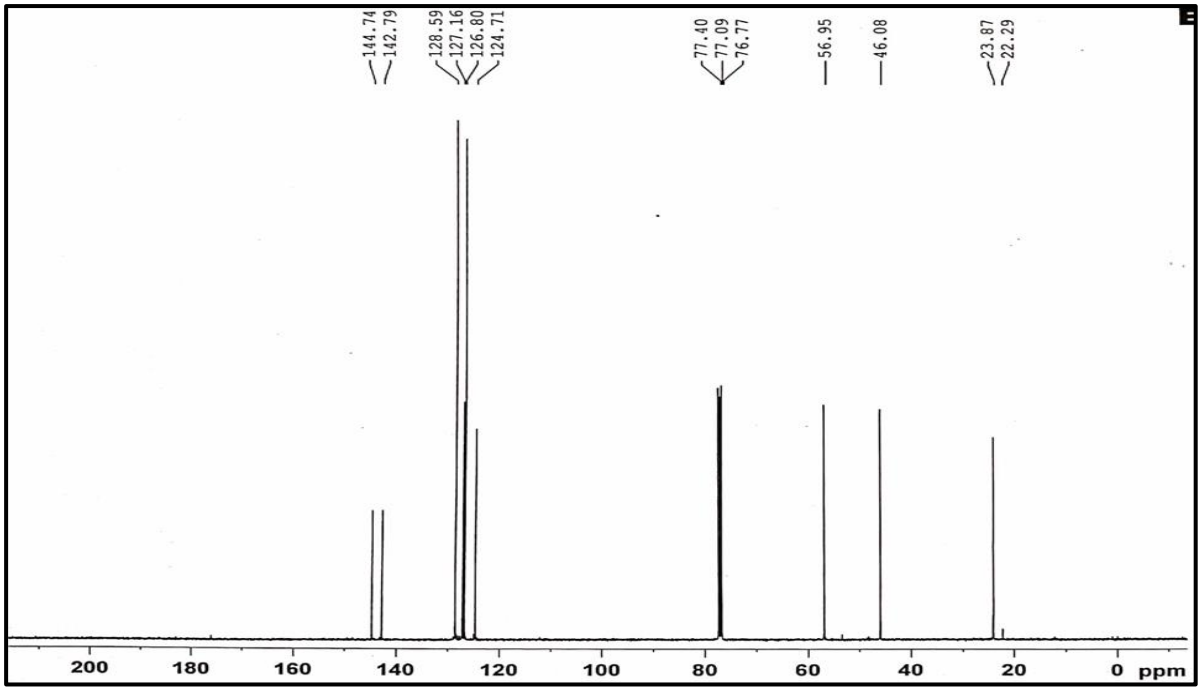

Annexure 15. ^{13}C NMR spectrum of **H_2L^3**.

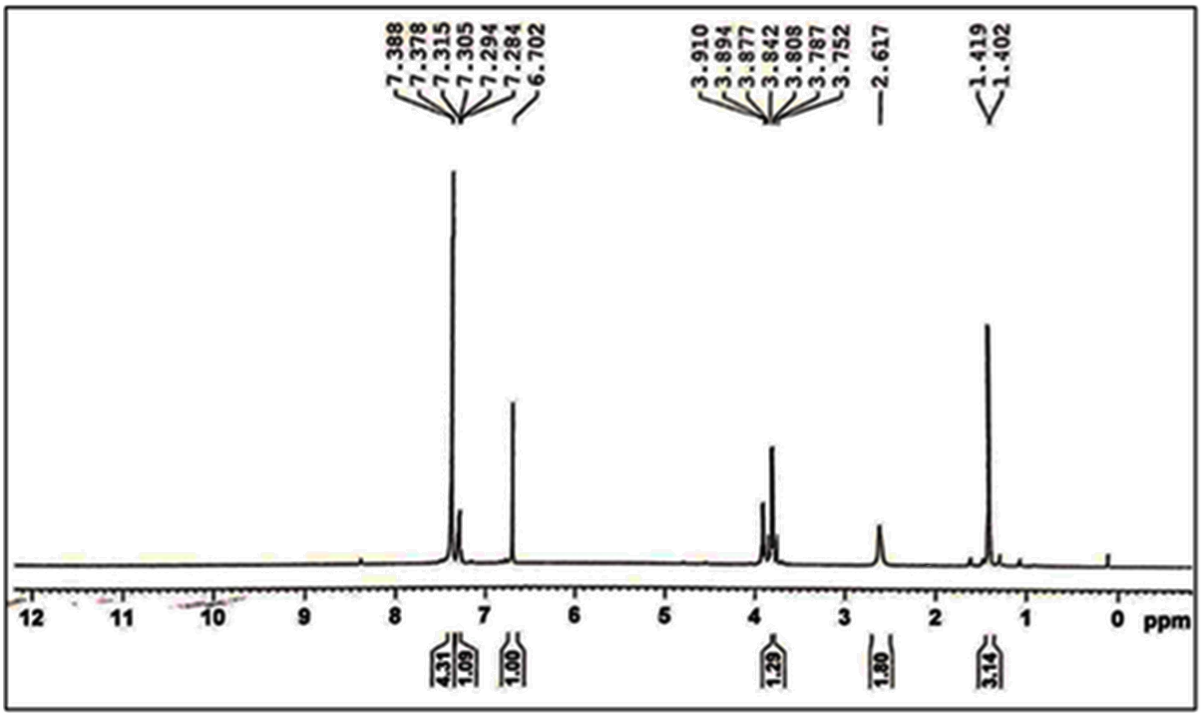

Annexure 16. ^{1}H NMR spectrum of **H_2L^4**.

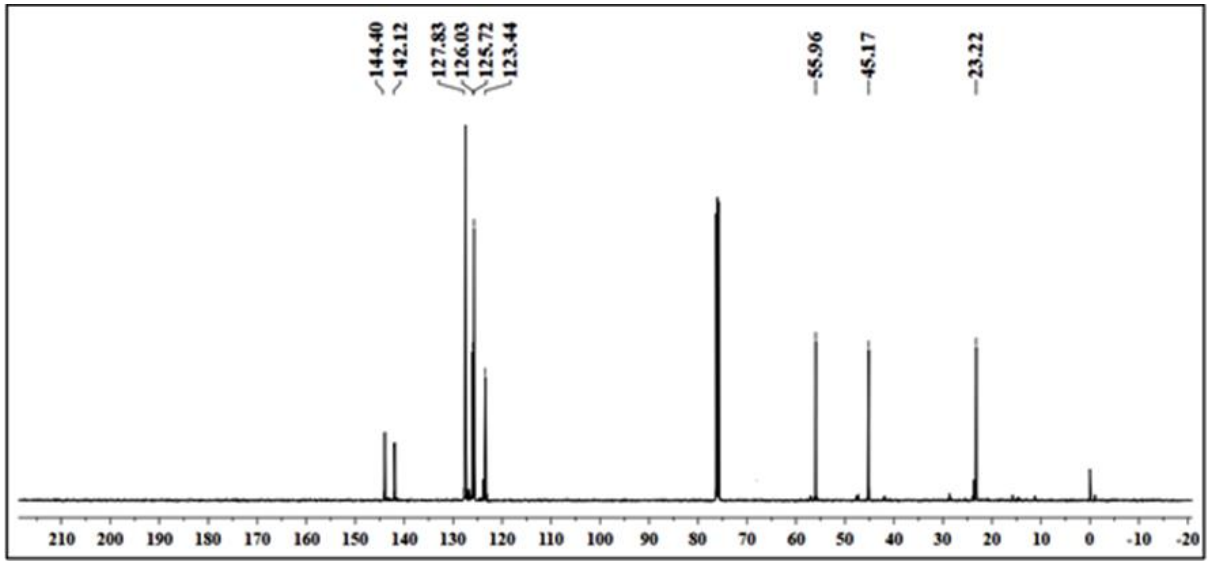

Annexure 17. ^{13}C NMR spectrum of **H_2L^4**.

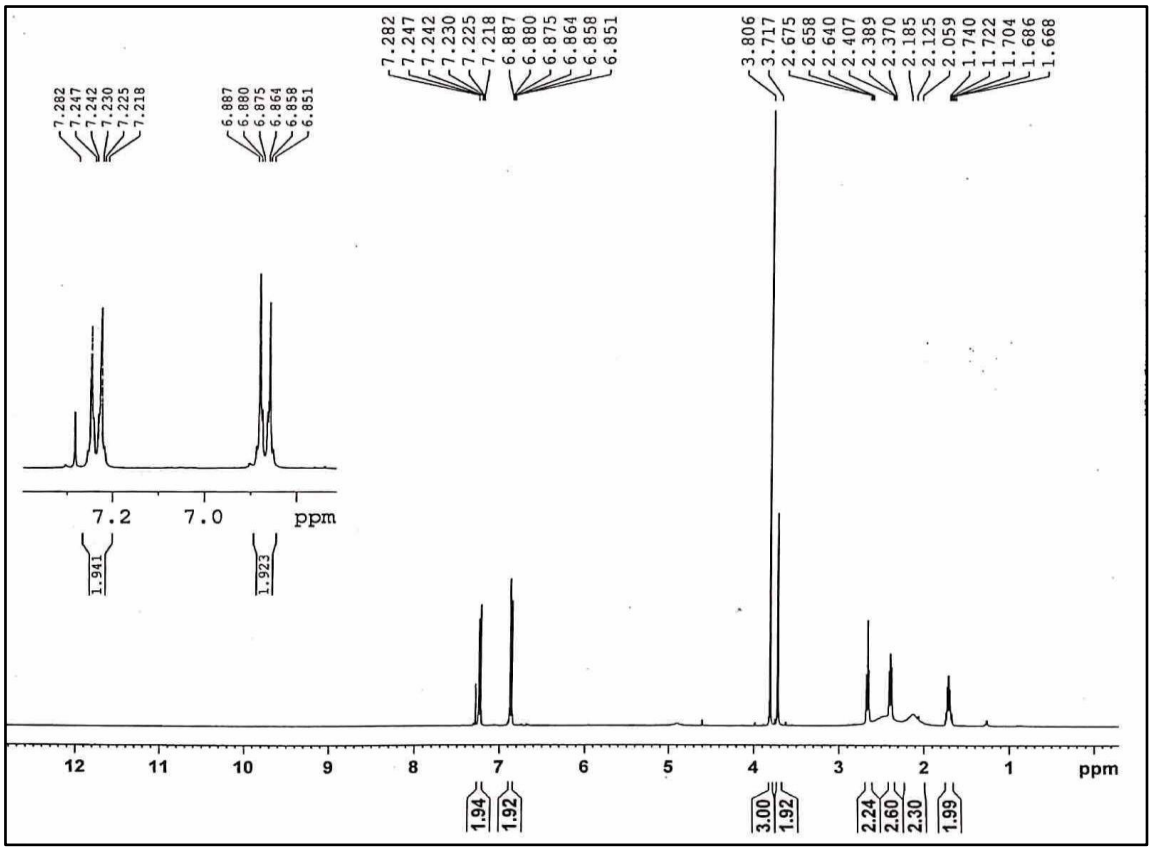

Annexure 18. ^{1}H NMR spectrum of **H_2L^5**.

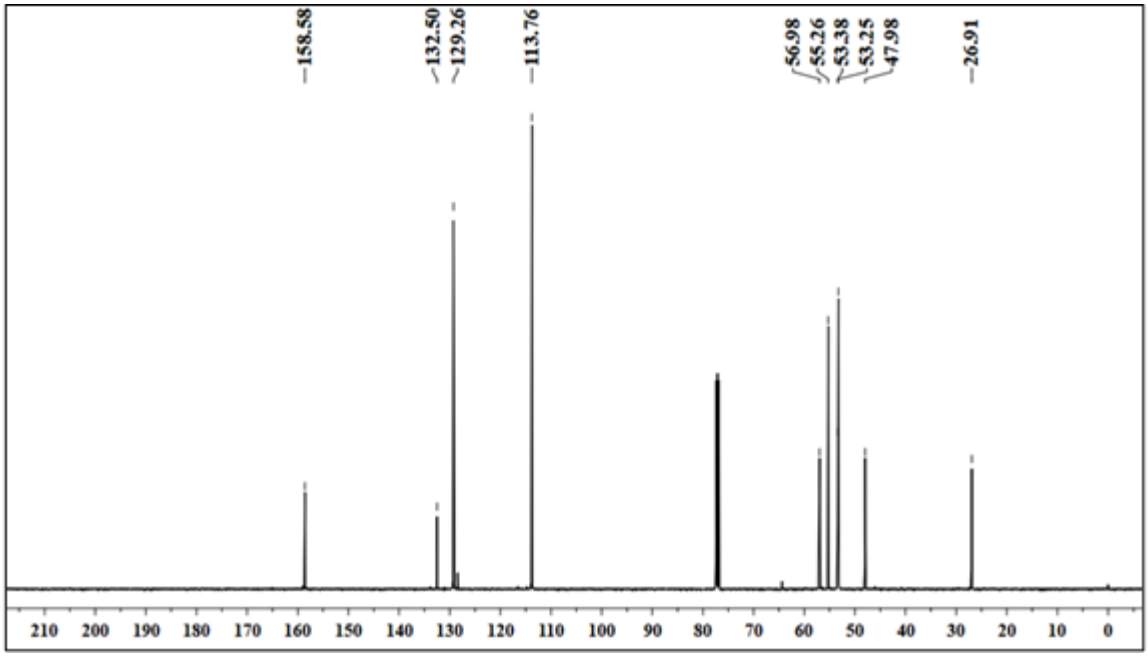

Annexure 19. ^{13}C NMR spectrum of **H_2L^5**.

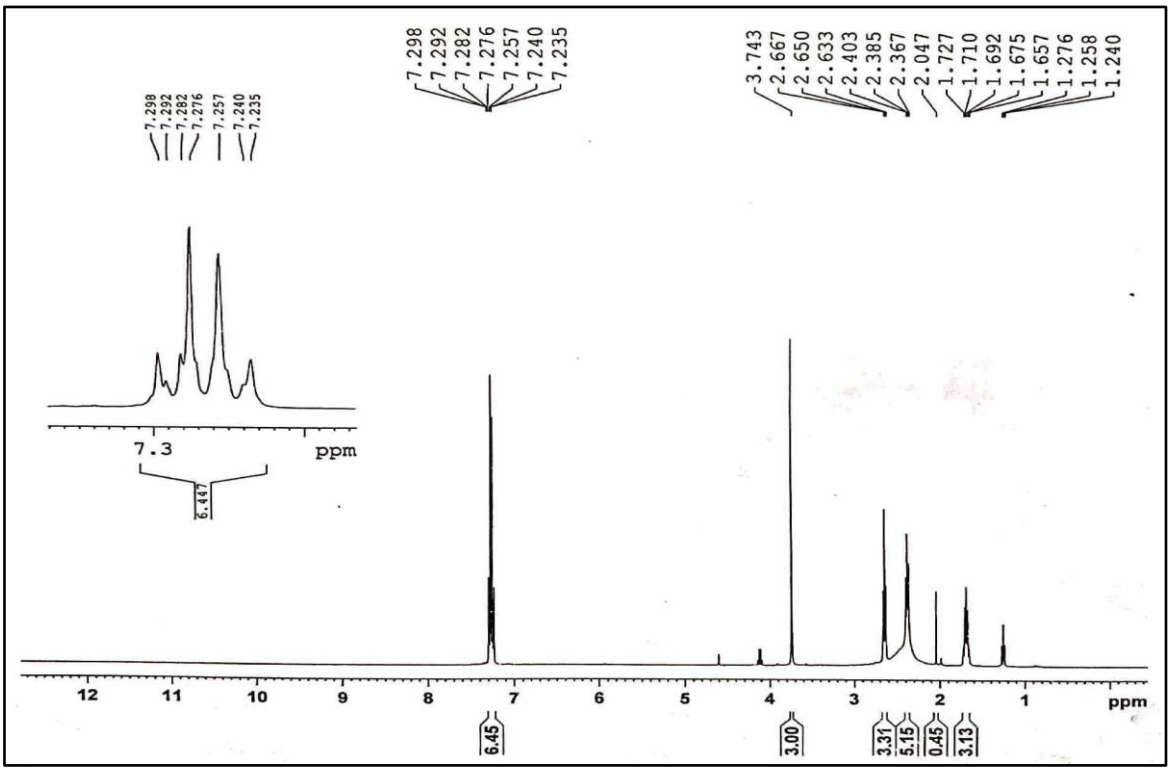

Annexure 20. ^{1}H NMR spectrum of **H_2L^6**.

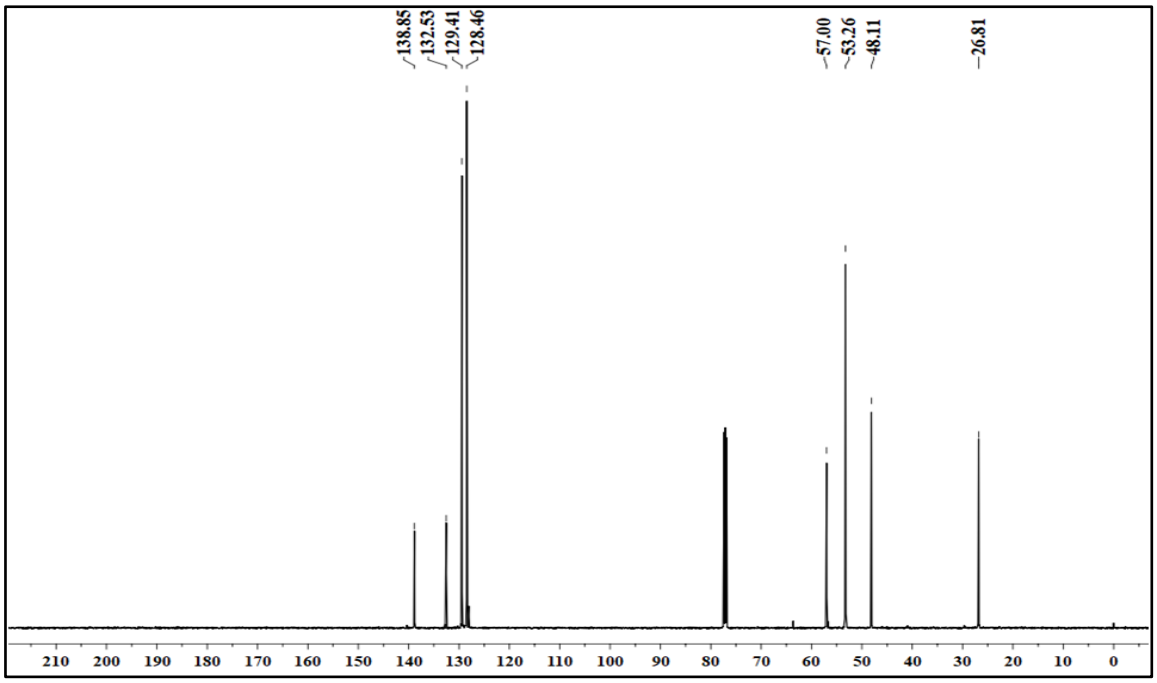

Annexure 21. ^{13}C NMR spectrum of **H_2L^6**.

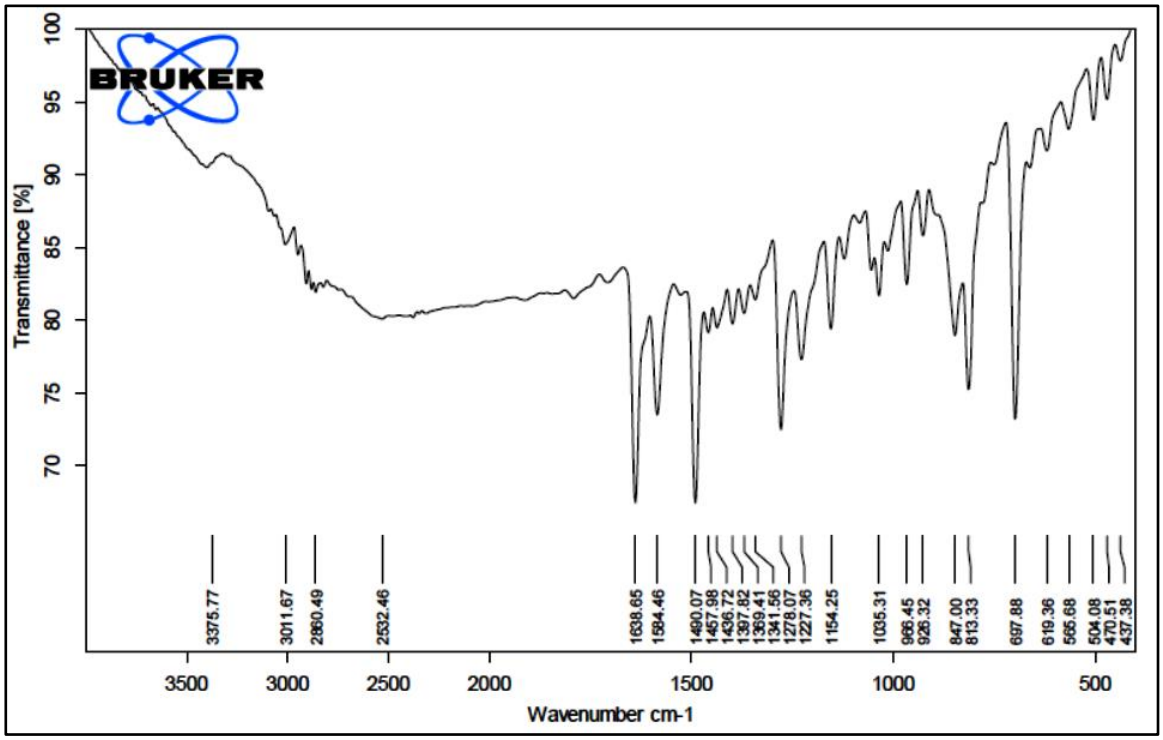

Annexure 22. FTIR spectrum of **BI-1**.

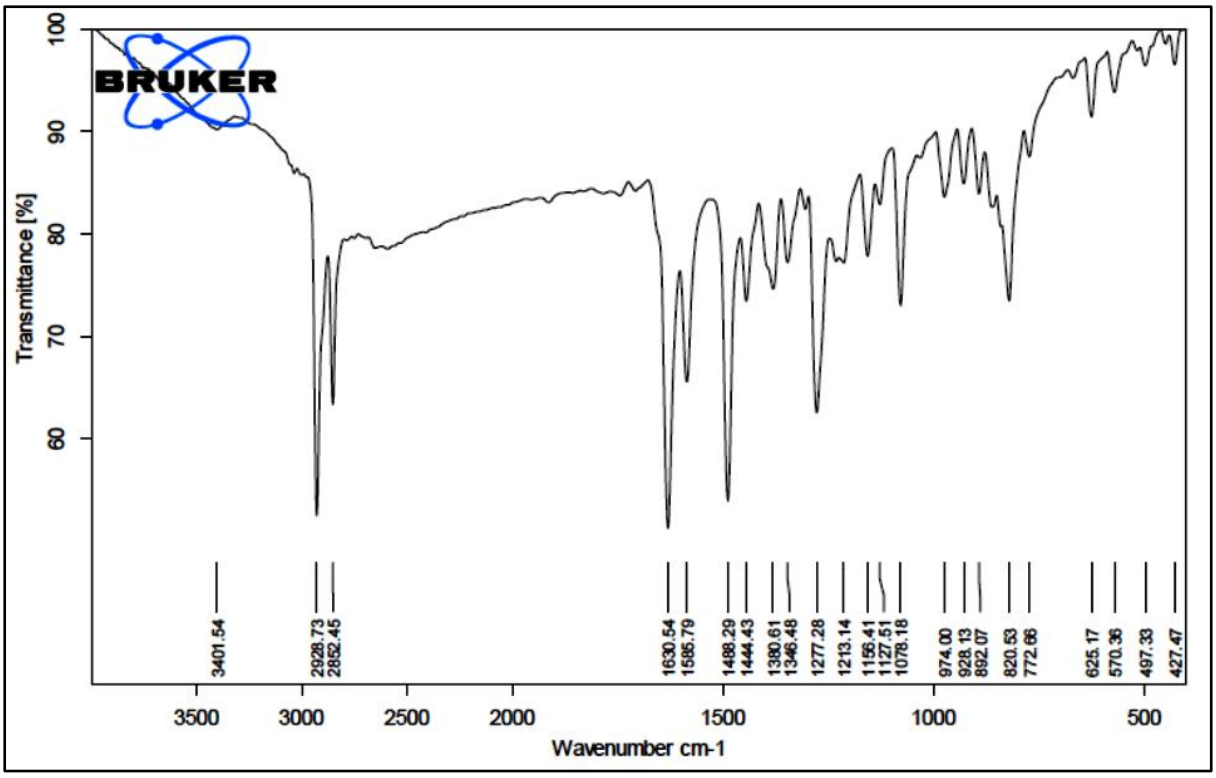

Annexure 23. FTIR spectrum of **BI-2**.

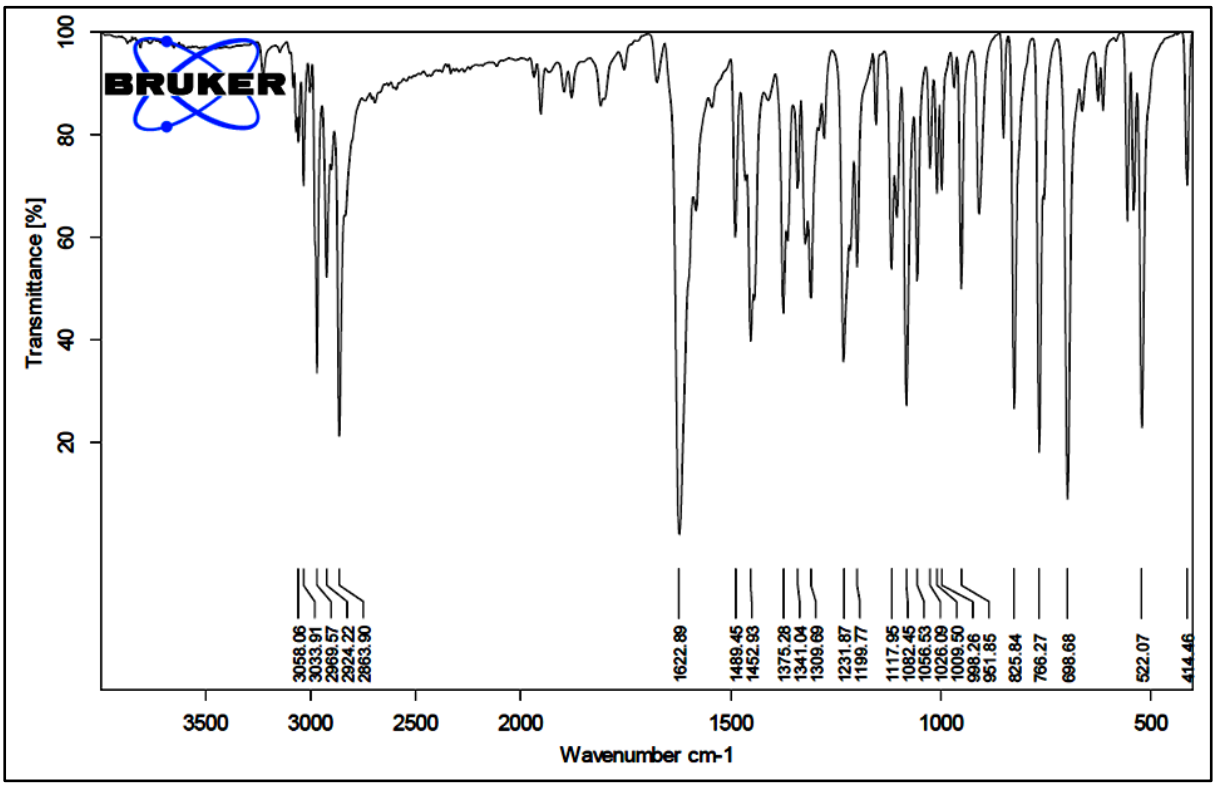

Annexure 24. FTIR spectrum of **BI-3**.

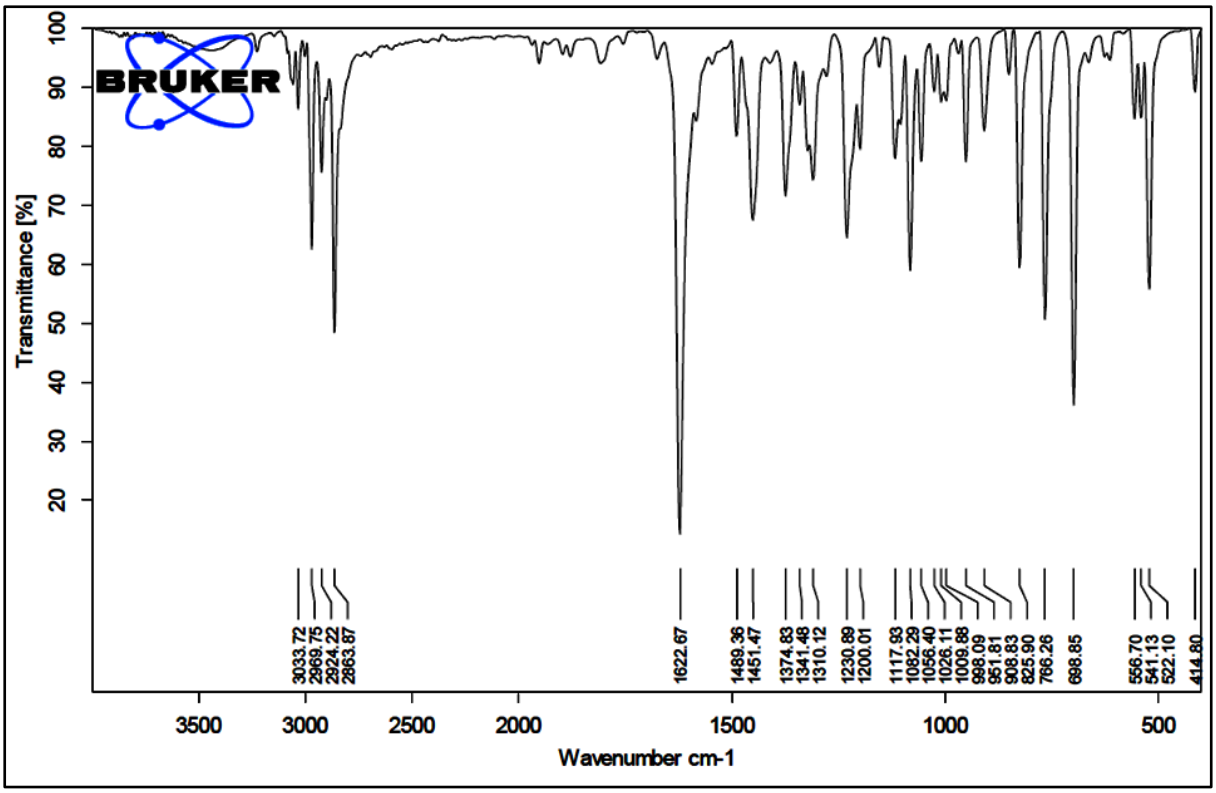

Annexure 25. FTIR spectrum of **BI-4**.

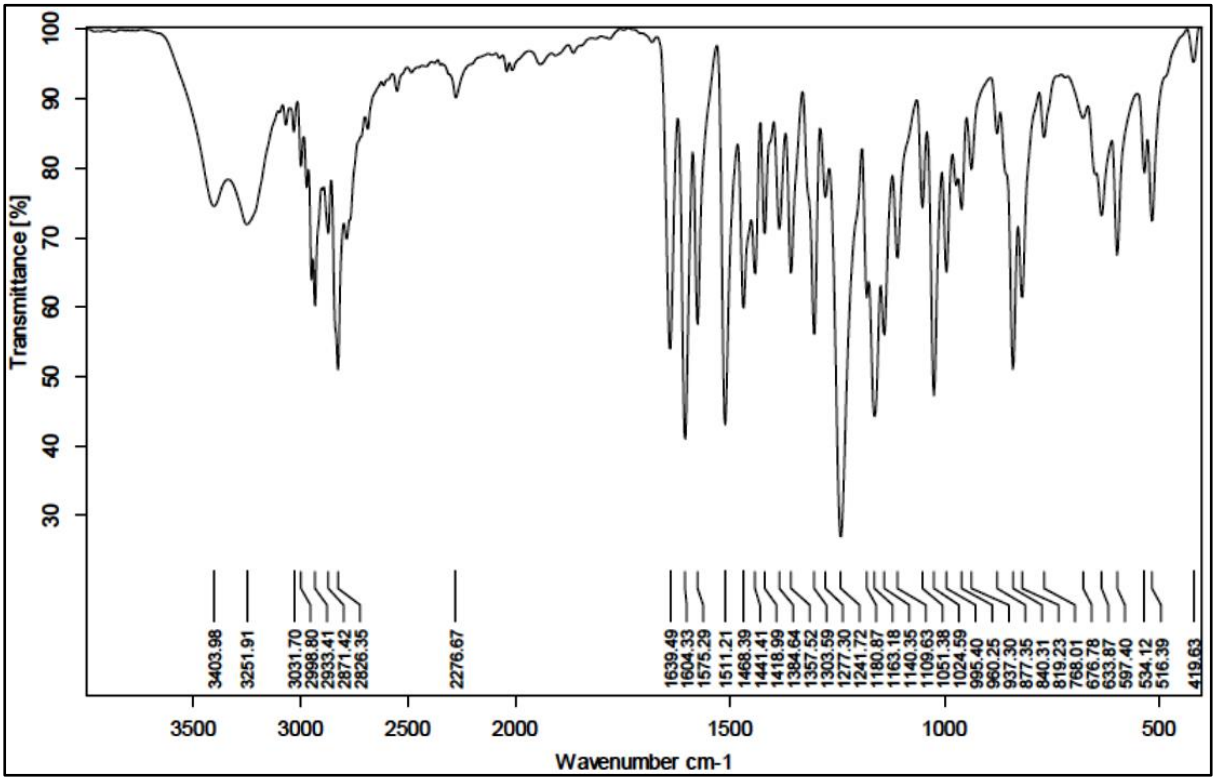

Annexure 26. FTIR spectrum of **BI-5**.

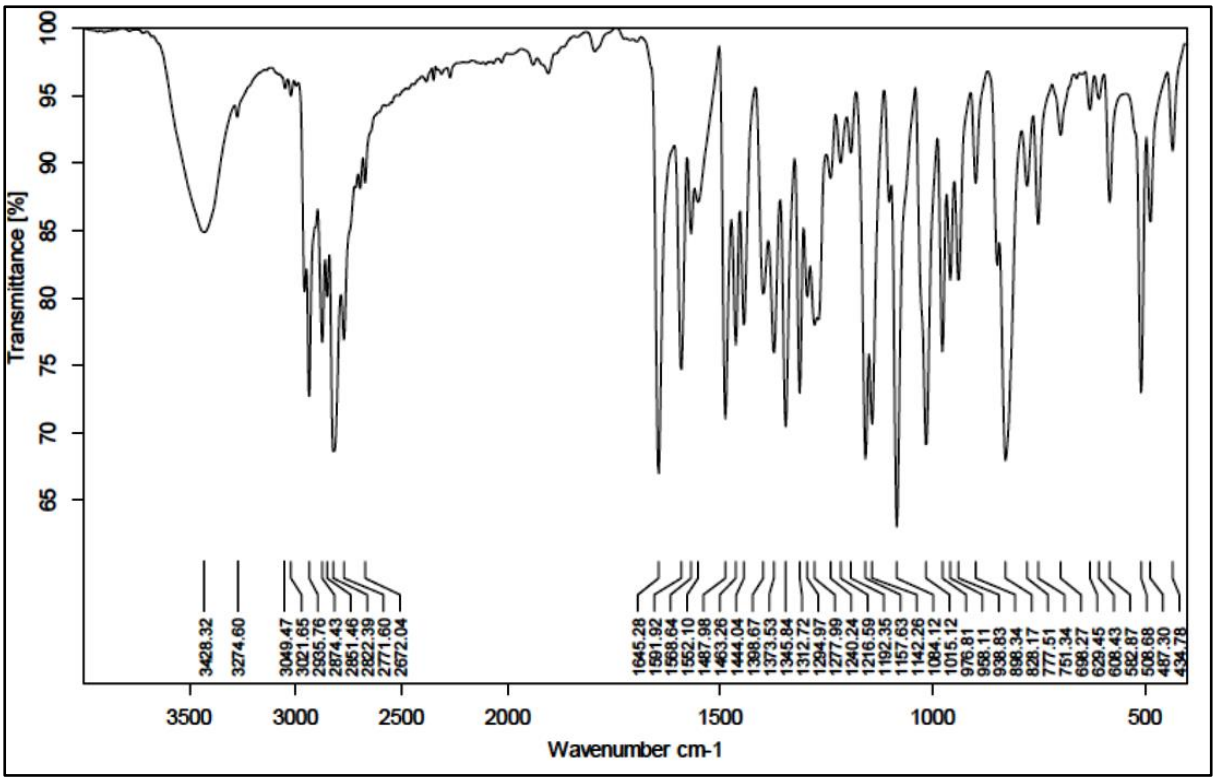

Annexure 27. FTIR spectrum of **BI-6**.

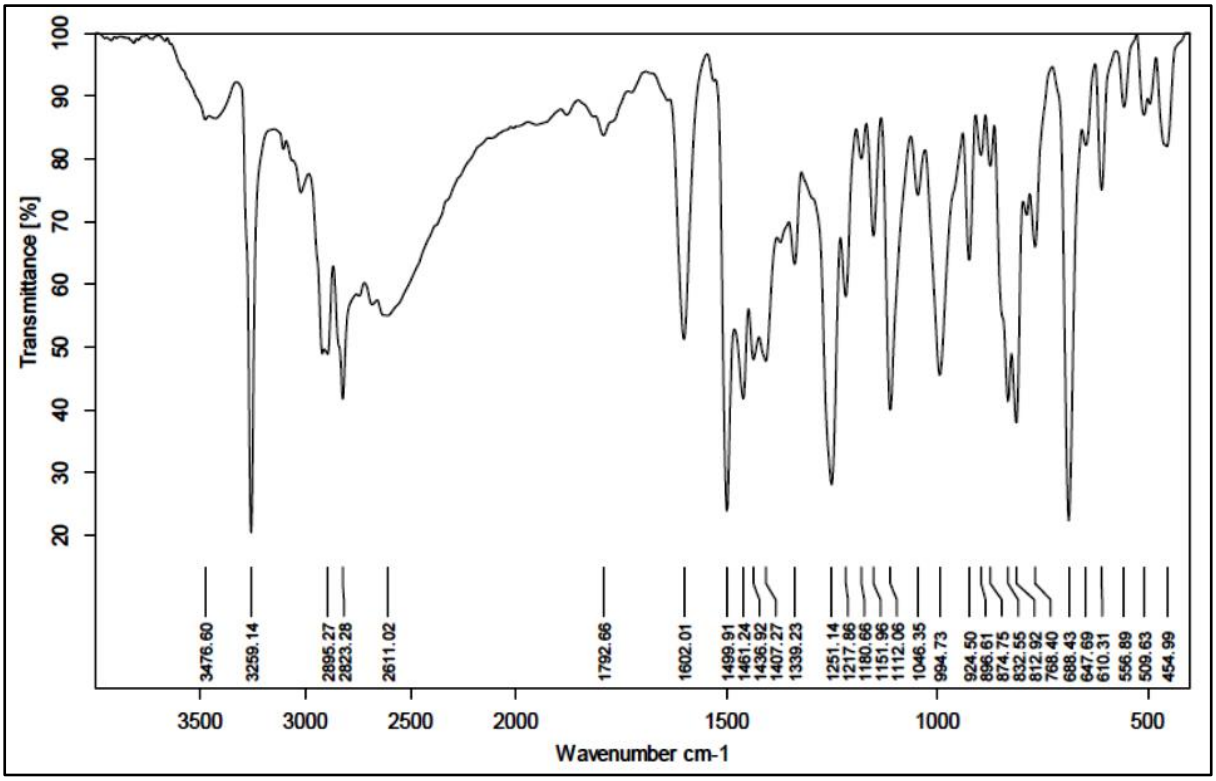

Annexure 28. FTIR spectrum of $\mathbf{H_2L^1}$.

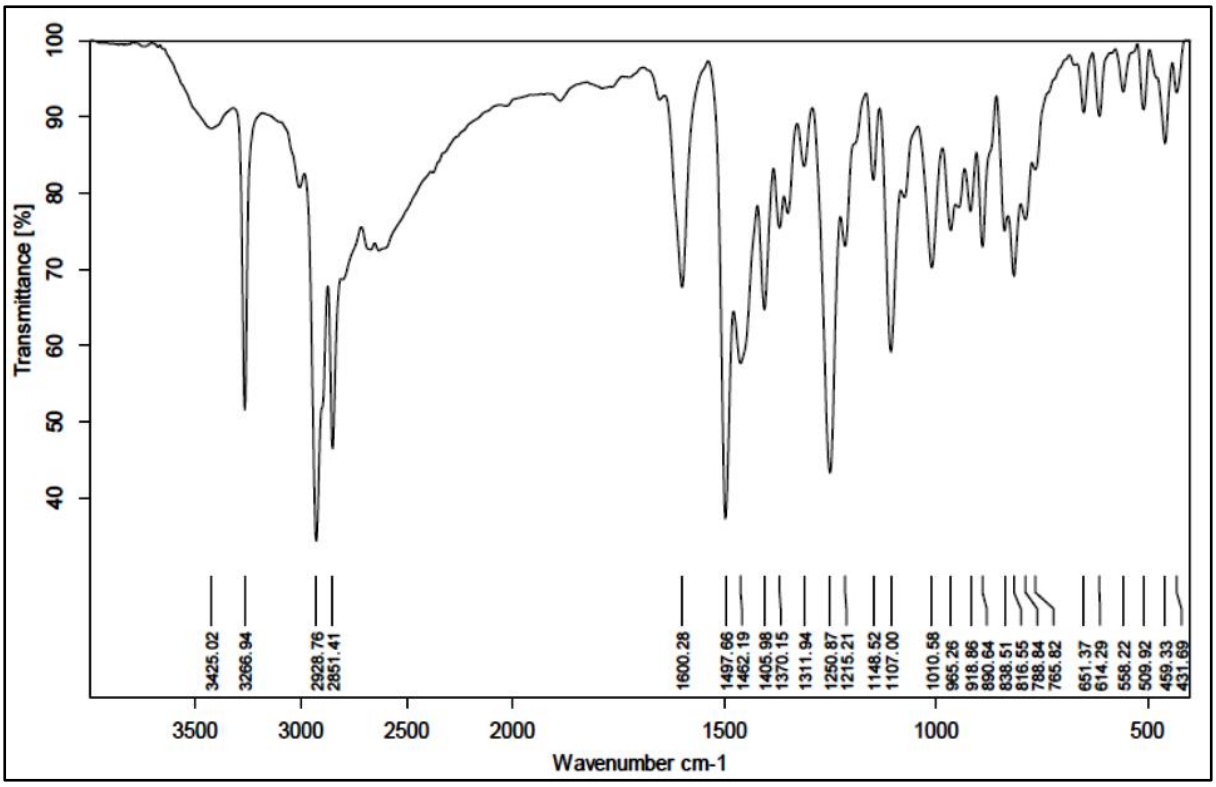

Annexure 29. FTIR spectrum of H_2L^2.

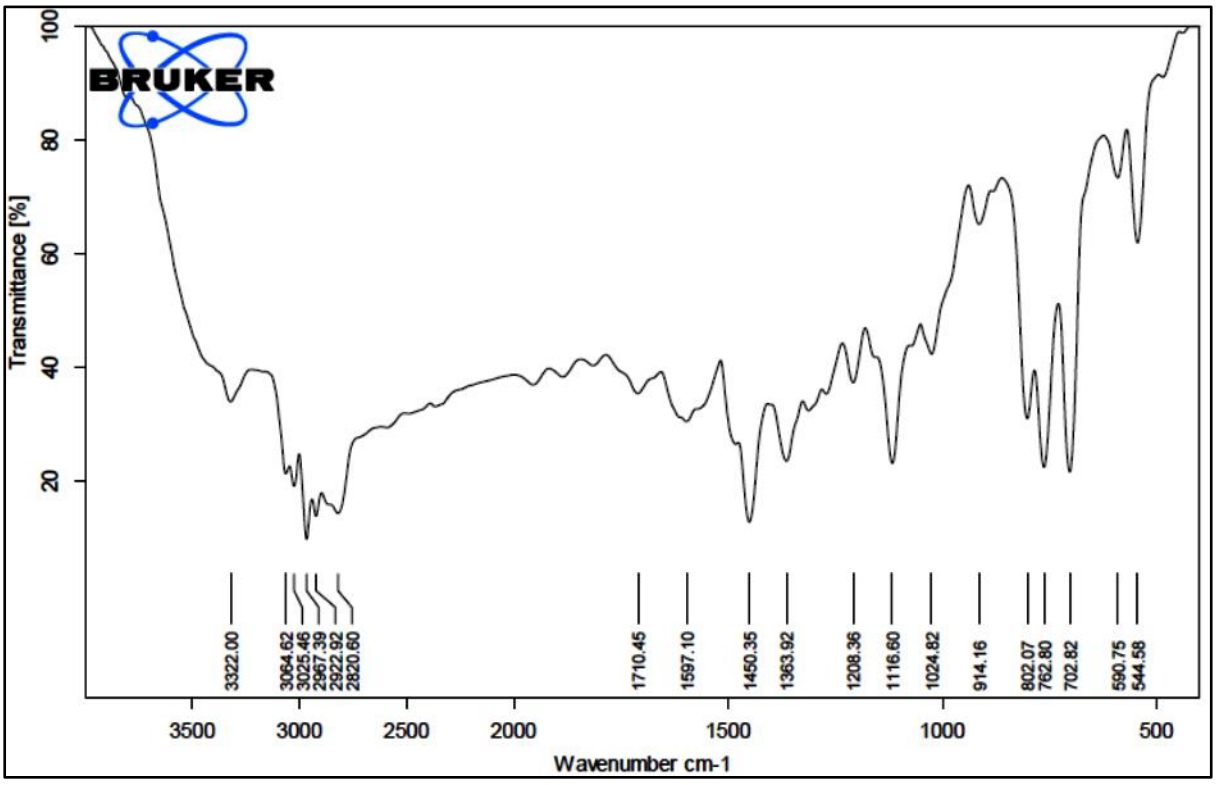

Annexure 30. FTIR spectrum of H_2L^3.

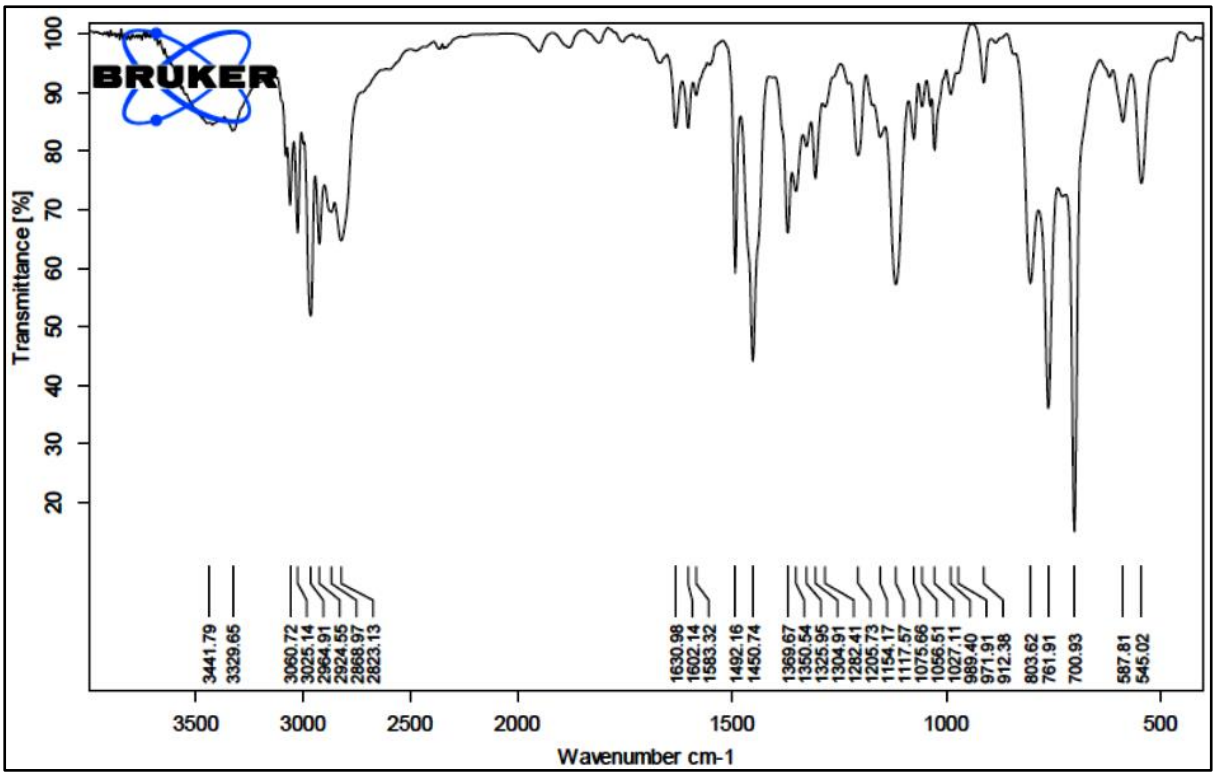

Annexure 31. FTIR spectrum of H_2L^4.

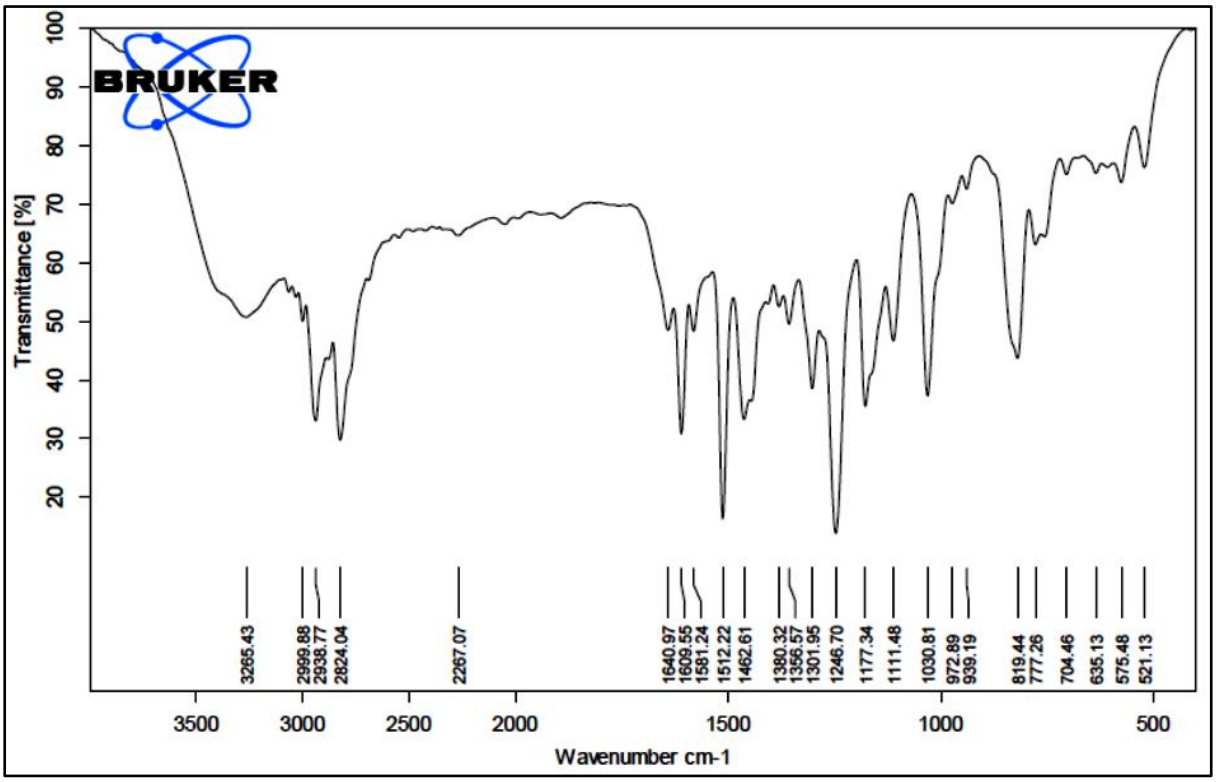

Annexure 32. FTIR spectrum of H_2L^5.

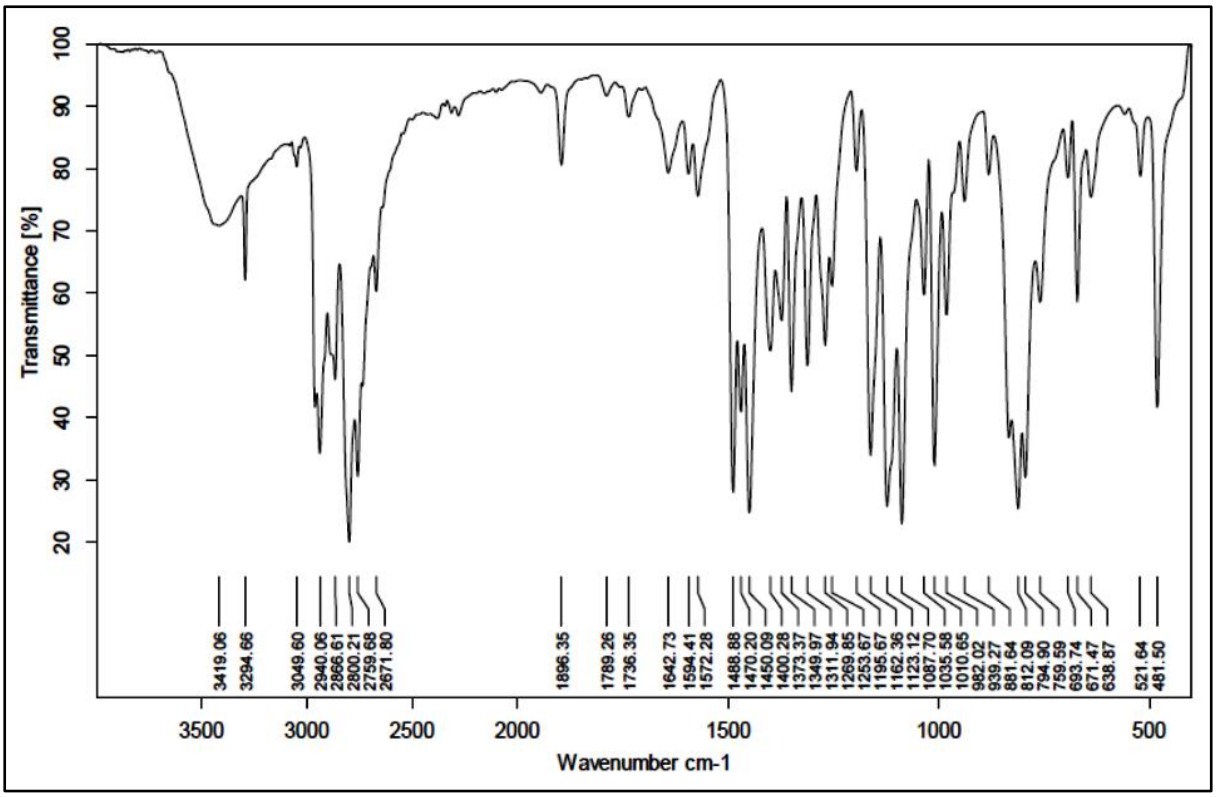

Annexure 33. FTIR spectrum of **H_2L^6**.